

Exoplanet Atmospheres at High Spectral Resolution

Ignas A. G. Snellen

Leiden Observatory, Leiden University, Postbus 9513, 2300 RA Leiden, The Netherlands

xxxxxx 0000. 00:1–50
Copyright © 0000 by Annual Reviews.
All rights reserved

Keywords

Exoplanets; atmospheres; spectroscopic techniques; planet formation; atmospheric chemistry; atmospheric dynamics

Abstract

High-resolution spectroscopy (HRS) has grown into one of the main techniques to characterise the atmospheres of extrasolar planets. High spectral resolving power allows for the efficient removal of telluric and host-star contamination. Combined with the large collecting area of ground-based telescopes it enables detailed studies of atmospheric species, temperature structure, atmospheric loss, and global winds and circulation patterns. In this review, the wide range of HRS observation and data-analysis techniques are described and literature results discussed. Key findings include:

- The highest irradiated planets show a rich spectrum of atomic and ionic species, just like stars.
- Retrieval analyses of Hot Jupiters and directly imaged Super-Jupiters point to Solar metallicities and chemistry, but observed samples are still heterogeneous and incomplete.
- There appears to be a clear dichotomy between Hot Jupiters with and without atmospheric inversions, depending on their equilibrium temperature.
- Some highly irradiated planets exhibit enormous leading and/or trailing tails of helium gas, providing unique insights into planet evolution and atmospheric escape processes.
- Minor isotopes of carbon and oxygen are now being detected in gas giant planets and brown dwarfs with the interesting potential to shed light on formation pathways.

A list of potential pitfalls is provided for those new to the field, and synergies with JWST are discussed. HRS has a great future ahead with the advent of the extremely large telescopes, promising to bring temperate rocky exoplanets into view with their increase in HRS detection speed of up to three orders of magnitude.

Contents

1. Introduction	2
1.1. A brief history of exoplanet atmospheric observations	3
1.2. Overview of high-resolution spectroscopic methods	5
2. Detailed techniques	8
2.1. HRS instrumentation	8
2.2. Observation and data analysis strategies	10
2.3. Atmospheric modelling	16
2.4. Potential pitfalls	18
3. Results on close-in exoplanets	20
3.1. Measurements of atoms, ions, and molecules	20
3.2. Atmospheric temperature structure	25
3.3. Atmospheric dynamics, rotation, and outflows	26
3.4. Reflected-light searches	31
3.5. Chromatic Doppler Shadow measurements	31
4. Results on wide-separation exoplanets	32
4.1. Molecular abundances and atmospheric temperature structure	32
4.2. Orbital and Rotational Dynamics	34
4.3. Isotope measurements	35
5. Synergies with JWST spectroscopy of exoplanets	36
6. Future opportunities with the ELT	38
6.1. Towards Earth-like planets	38

1. Introduction

Since the discovery of the first extrasolar planets in the early 1990s, thousands of new worlds have been discovered. While the census of planetary systems is yet far from complete, it is clear that exoplanets are both common and diverse. They can be found in orbits of less than a day, but also at hundreds of astronomical units from their host star, and their masses and radii point to a broad continuum in compositions. Evidently, our Solar System is not a universal blueprint for other planetary systems.

An important goal of exoplanet studies is to understand the formation and evolutionary processes driving this diversity. This will also enlighten us about the worlds in our own Solar System, e.g. explain why Earth and Venus are so different, or how planetary climates have evolved over time. Only by studying a wide variety of worlds, over a wide range of orbits, host-star properties, ages, and compositions, will we be able to identify families or classes of planets and understand their formation and evolutionary relationships. This has also a strong philosophical component with a unique opportunity to learn about ourselves as highly-evolved organisms living on a temperate, water-rich world. How common are life-bearing planets? Are there any other worlds like Earth?

Some basic properties of exoplanets can be constrained using indirect detection methods, such as planet mass from radial velocity measurements, radius from transit observations, and mean density from the combination of the two. The latter can put constraints on a planet's bulk composition, but solutions are often highly degenerate and atmospheric measurements are required to gain more detailed knowledge on chemical make-up and local conditions. The first question that can be addressed is whether a planet has an atmosphere

or not. Subsequently we want to know its chemical ingredients and temperature structure. Do we understand the physical and chemical processes in the context of its formation and evolution? In the search for habitable environments and extraterrestrial life we want to know whether there is evidence for water. Can we detect any potential biomarker gases, such as molecular oxygen, ozone, or methane? And ultimately, are these biomarkers indeed due to biological activity?

While space-based observations have kick-started the field of atmospheric characterisation more than two decades ago, ground-based high-resolution spectroscopy (HRS) has slowly but surely developed into a remarkable and unique way to probe exoplanets and forms the focus of this review. In the remainder of Section 1, a brief history of exoplanet atmospheric observations is presented, followed by an overview of the wide range of HRS observing methods. Section 2 provides technical details on HRS instrumentation, data acquisition, signal search-techniques, and retrieval analyses. Section 3 discusses results for short-period planets that have been presented in the literature so far using HRS transmission and phase-curve measurements. Section 4 discusses these for directly-imaged planets for which HRS is combined with high-contrast imaging techniques. Section 5 examines synergies with JWST observations, and Section 6 discusses the exciting future of HRS in the era of the Extremely Large Telescopes.

A graduate-level review on high-resolution spectroscopy for exoplanet atmospheres has been presented before by Birkby (2018). The general review on exoplanet atmospheres by Madhusudhan (2019) is also a great source of information.

1.1. A brief history of exoplanet atmospheric observations

After the discovery of two planetary-mass objects orbiting a pulsar (Wolszczan & Frail 1992), it was the detection of the first hot Jupiter by Mayor & Queloz (1995) that started a genuine scientific revolution. Significant skepticism existed in early days, since it was not generally accepted that the observed radial velocity variations were caused by orbiting planets (e.g. Gray 1997). This resulted in a strong incentive to search for other evidence for exoplanets, in particular starlight scattered off their atmospheres (Charbonneau et al. 1999, Collier Cameron et al. 1999). Although unsuccessful, these attempts constitute the first time HRS was utilised to search for atmospheric signals. At high spectral resolution, reflected light can be disentangled from direct starlight due to its Doppler shift caused by the orbital motion of a planet. Unfortunately, hot Jupiters turn out to have very low albedos and no undisputed HRS scattered-light signals have been found so far.

The groundbreaking discovery that the hot Jupiter HD 209458 b transits its host star (Charbonneau et al. 2000) opened the way for a new technique: exoplanet transmission spectroscopy (Seager & Sasselov 2000). Subsequently, Charbonneau et al. (2002) detected sodium in transmission using the HST STIS spectrograph, the start of a new subfield of exoplanet atmosphere measurements. In the years that followed, space-observations with both HST and Spitzer Space Telescope were trail-blazing. Charbonneau et al. (2005) and Deming et al. (2005b) presented the first secondary eclipse measurements of thermal emission using Spitzer, followed by the first infrared phase-curve and longitudinal heat-distribution (Knutson et al. 2007). HST observations in ultra-violet light showed significant Ly α and metallic transmission signals out to at least several planet radii, pointing to exospheric absorption and atmospheric loss processes (Vidal-Madjar et al. 2003, 2004). Absorption from water vapour turned out to be more elusive, and early claims (e.g. Tinetti et al. 2007) were

disputed, until water measurements became irrefutable with HST’s WFC3 instrument (e.g. Deming et al. 2013). HST has been pushing the frontier of atmospheric characterisation up to the launch of JWST (see Section 5), by inferring hazes from hot-Jupiter spectra (Sing et al. 2016), high-precision transmission spectroscopy of the mini-Neptune GJ 1214 (Kreidberg et al. 2014) and cool planets such as K2-18b (Benneke et al. 2019), and many other results.

In the meantime, theoretical studies showed the exciting possibilities of ground-based HRS transmission spectroscopy (e.g. Brown 2001), but early attempts resulted in upper limits (Wiedemann et al. 2001, Moutou et al. 2001, Deming et al. 2005a). The first successful ground-based observations targeted the sodium D lines in HD 189733 b and HD 209458 b using the Hobby-Eberly Telescope (Redfield et al. 2008) and Subaru Telescope (Snellen et al. 2008) respectively, the latter confirming the earlier HST detection. While sodium has been detected in many Hot Jupiters since, recent observations of HD 209458 have cast some doubts on these early results (Casasayas-Barris et al. 2021, see Section 3.1), mostly due to the treatment of stellar-related contaminants.

Subsequently, the CRIRES spectrograph on ESO’s Very Large Telescope was used to detect carbon monoxide in the transmission spectrum of HD 209458 b (Snellen et al. 2010), successfully utilising cross-correlation techniques for the first time. It demonstrated the unique capabilities of HRS compared to space-based low-resolution spectroscopy by the unambiguous detection of a molecular signal, and revealing Doppler effects of planet orbital motion and possible atmospheric winds. The change in the radial component of the orbital velocity of a planet was subsequently used to target thermal emission of the non-transiting planet τ Bootis b (Brogi et al. 2012, Rodler et al. 2012), detecting carbon monoxide and revealing its orbital inclination, followed by the first ground-based detection of water in the thermal spectrum of HD 189733 b (Birkby et al. 2013).

An alternative route to characterise exoplanet atmospheres opened up through the first detections of substellar companions using high-contrast imaging (HCI; e.g. Chauvin et al. 2004, Marois et al. 2008, Lagrange et al. 2010). These Super-Jupiters are typically massive gas giants that straddle the planet/brown-dwarf divide residing on wide orbits in young (<100 Myr) star systems, and are almost solely in the observational realm of large ground-based telescopes with state-of-the-art adaptive optics systems. Since every measurement directly probes such object, atmospheric characterisation is immediate upon discovery and can be supplemented by observations at different wavelengths or high-contrast spectroscopy. In this way, the dominant spectroscopically-active species are readily observable in Super-Jupiters, such as water, carbon monoxide, and methane (e.g. Bowler et al. 2010), in addition to constraining the atmospheric temperature structure and possible presence of clouds. Since the spectroscopic signatures of stars and their planets are significantly different, many studies have recognised the power of combining high-contrast imaging with high-resolution spectroscopy (e.g. Sparks & Ford 2002, Riaud & Schneider 2007, Kawahara & Hirano 2014, Snellen et al. 2015). Konopacky et al. (2013) first demonstrated the strength of medium-resolution integral-field spectroscopy on the HR8799 system with the 10m Keck OSIRIS spectrograph. Subsequently, CRIRES was used to target the massive gas-giant Beta Pictoris b, measuring the radial component of its orbital velocity and deriving its spin-rotation period via its $v \sin i$ (Snellen et al. 2014).

Over the years, HRS has developed into an established observational technique for exoplanet atmospheric characterisation. In the current JWST era, which provides unprecedented and unrivalled capabilities in particular in the thermal infrared, ground-based HRS

remains uniquely competitive and highly synergetic with space-based observations (see Section 5). E.g., HRS observations show that the optical spectra of the highest irradiated gas giants are dominated by neutral and ionised metals (Hoeijmakers et al. 2019), with dayside spectra suggesting strong thermal inversions (Nugroho et al. 2020a). Atmospheric escape processes can now be probed very effectively at high spectral resolution using the helium 1083 nm line (Allart et al. 2018, Nortmann et al. 2018). A strong synergy is developing between spatially resolved HRS observations that reveal signatures of day-night winds, zonal flows, and other atmospheric dynamics, and 3D atmospheric modelling (Louden & Wheatley 2015). HRS spectroscopy of directly-imaged Super-Jupiters have allowed for the first isotope measurements (Zhang et al. 2021). As discussed in Section 6, soon the Extremely Large Telescopes will further revolutionise the field of HRS atmospheric characterisation, ultimately opening up to temperate rocky planets.

1.2. Overview of high-resolution spectroscopic methods

Any atmospheric measurement requires radiation originating from the planet to be distinguished from that of the host star. Basically, two families of methods achieve this: either through time-differential observations where contributions from the planet change over time (e.g. during transit, eclipse or with phase-curve observations - technical details discussed in Section 2.2), or by angularly separating the planet from the star (e.g. direct, high-contrast imaging or interferometric observations). Figure 1 shows a diagram (c.f. Perryman 2000) of the wide range of methods in which HRS is used to target exoplanet atmospheres, and which properties can be measured now or possibly in the future.

Transmission spectroscopy measures the integrated light from the planet-star system during transit as function of wavelength (e.g. Madhusudhan 2019). Absorption and scattering processes make the transparency of the atmosphere dependent on wavelength, and as such impact the effective planet size and transit depth. With HRS, the transmission spectrum is also sensitive to Doppler effects induced by the planet orbital motion and atmospheric dynamics such as day-to-nightside winds, equatorial jet-streams, or bulk-rotation. The transmission signal from a specific atmospheric species depends on its abundance as function of altitude in the atmosphere, the abundances of other species that may shield its signal, and the atmospheric temperature structure which is influenced by the surface gravity and mean molecular weight of the atmosphere. In the UV-optical, transmission signals generally come from atoms and ions originating from the hydrostatic part of the atmosphere or an extended exosphere that may indicate atmospheric escape. Transmission spectroscopy in the near-infrared is mainly sensitive to molecular absorption, but exospheric helium can also be targeted.

During transit, the Rossiter-McLaughlin effect (RM or Doppler shadow) induced by a planet, which is widely used to measure spin-orbital alignments, can also be used to obtain a transmission spectrum (Snellen 2004, Dreizler et al. 2009, Santos et al. 2020). The amplitude of the RM effect (measured using stellar lines) depends on the effective size of the planet, which is affected by atmospheric absorption and scattering as above. By measuring chromatic variations in the RM-effect, broad-band transmission features can be determined, which are mostly inaccessible via classical HRS transmission spectroscopy. During transit, information can also be obtained on the spectrum of the local stellar surface that is being transited, such as star spots and center-to-limb variations (CLV) in stellar line shapes and strengths (Cegla et al. 2016). The combined effects of the Doppler shadow, CLV, and planet

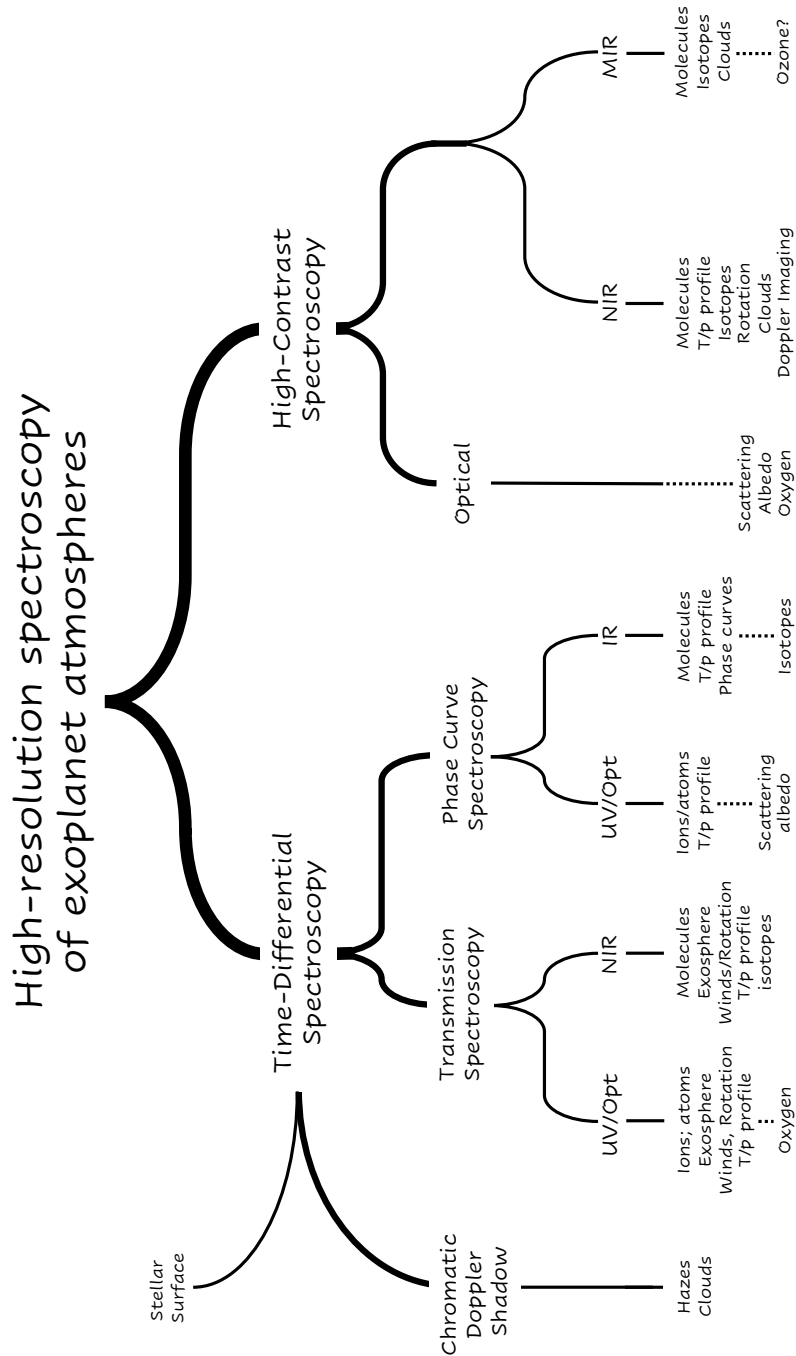


Figure 1

Diagram showing the range of methods employed to probe exoplanet atmosphere using high-resolution spectroscopy. The specific atmospheric properties that can be studied are indicated per wavelength regime. Dotted lines indicate future possibilities (c.f. Perryman 2000).

atmospheric absorption can be very challenging to disentangle.

Phase-curve observations are time-differential measurements away from the transit, during which the planet is seen from different viewing angles. In contrast to transmission spectroscopy, non-transiting planets can also be targeted. While in the latter case constraints on the planet radius are missing, the HRS phase-curve yields the orbital inclination of the planet and therefore the true mass. As for transmission spectroscopy, infrared phase-curve observations are dominated by molecular opacity sources. The temperature structure, i.e. temperature-pressure (T/p) profile of the atmosphere, governs how molecular opacity is translated into the observed spectrum. An isothermal atmosphere produces (to first order) a black body spectrum without atomic or molecular lines. An atmosphere with an inverted or non-inverted T/p profile results in emission or absorption lines respectively. In the UV/optical the contrast between thermal emission from the planet and the star is generally very large. Only the hottest planets (i.e. Ultra-Hot Jupiters; UHJ), can currently be studied in this way. They show mainly opacity from atoms and ions, but potentially also metal-oxides and metal-hydrides. For all but the hottest planets the UV/optical light will likely be dominated by star-light scattered off the planet, but no undisputed HRS detections have yet been presented in the literature. If the size of the planet is known (i.e. for transiting planets), scattered light will lead to the geometric albedo of the planet as function of wavelength, providing insights in scattering processes (Rayleigh, Mie) and possibly the scattering medium (clouds, hazes, molecules). Depending of the effective range of altitudes at which the starlight is being scattered, light travels back and forth through the planet atmosphere, but is also being absorbed, meaning that also the scattered light spectrum will contain information on atmospheric constituents.

In the case of high-contrast spectroscopy (branch to the right of Fig. 1), high-contrast imaging techniques are combined with HRS. Light from the star is removed as much as possible at the position of the planet to obtain its spectrum free from stellar contamination. It requires an adaptive-optics-assisted HRS spectrograph, possibly in conjunction with coronagraphy. In principle, this technique can also be used in combination with interferometry, but no HRS modes yet exist for such instruments. So far, all directly-imaged planets amenable to HRS observations have more favourable star/planet contrasts because they are young and still warm from their formation. Since they are only detectable in relatively wide orbits, their spectra are completely dominated by thermal emission, and reflected starlight is negligible. As with phase-curve observations, their HRS spectra provide information on molecular species, atmospheric T/p profile, and the possible presence of clouds. Recently, the first isotopic measurements have also been obtained (Zhang et al. 2021). Planet spin-rotation can be constrained using line broadening. Potentially, spatially resolved information of planets may be obtained, revealing possible dark or bright spots or bands, using Doppler imaging (Crossfield 2014). These will require highly accurate HRS spectral time series.

In the era of the Extremely Large Telescopes (ELTs), HRS instrumentation will improve sufficiently to target planets around our nearest neighbour stars in reflected light, providing constraints on albedo and atmospheric constituents at optical/NIR wavelengths. Arguably the holy grail in exoplanet science is the search for extraterrestrial life via biomarker gases. Molecular oxygen is potentially detectable in atmospheres of nearby rocky exoplanets either using HRS transmission spectroscopy or high-contrast spectroscopy (e.g. Lovis et al. 2017).

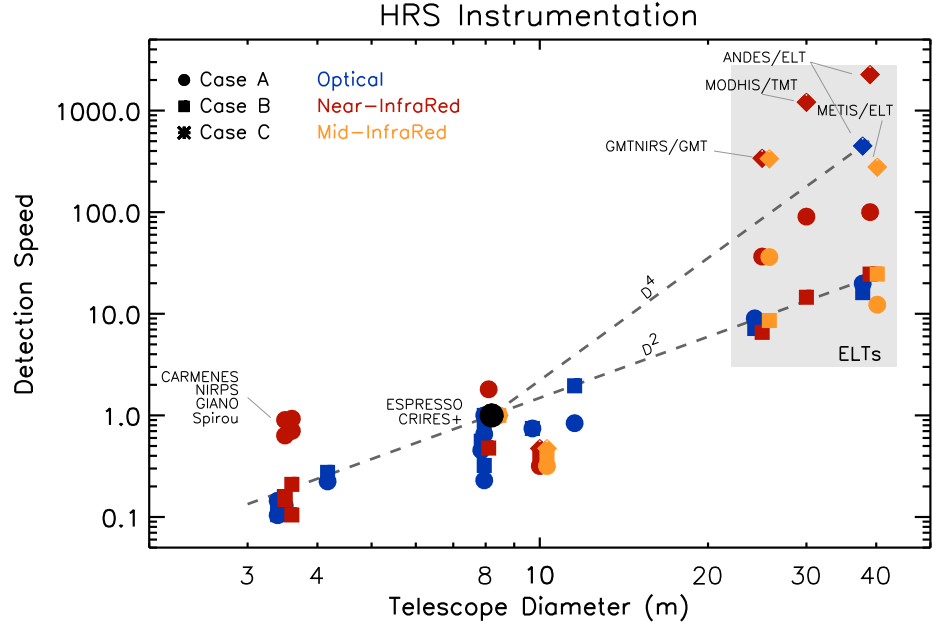


Figure 2

Detection speed of HRS observations for current and planned HRS instrumentation, normalised to the ESPRESSO (optical) and CRIRES+ (IR) spectrographs on ESO’s VLT. Three cases are specified (A, B, and C) as explained in the main text. ELT instrumentation will be up to three orders of magnitude faster than any instruments available now.

2. Detailed techniques

In this section, HRS observing and data analysis techniques are described in detail. Firstly, the relevant properties of HRS instrumentation are discussed, how they influence detection speed, and how existing and planned HRS instruments compare to each other. Section 2.2 reviews observation and data analysis strategies, Section 2.3 the many aspects of atmospheric modelling, and Section 2.4 provides a list of potential pitfalls.

2.1. HRS instrumentation

Over the past decades, there has been an enormous incentive to develop stable, high-precision, high-resolution spectrographs for the search of extrasolar planets using the radial velocity technique. These same instruments are utilised for exoplanet atmospheric observations. Only in recent years have instruments been developed with atmospheric work as their main science driver (e.g. Mawet et al. 2016, Vigan et al. 2024). A key property is the detection speed, Γ , which governs the observing time needed to achieve a detection of a certain atmospheric species at a set signal-to-noise (S/n) ratio. Here, three very simplified cases, A, B, and C, are discussed.

In Case A, the target spectrum consists of a set of well-separated, infinitely narrow lines of equal strength. Assuming a telescope diameter D and a telescope + instrument throughput of f , the detection speed is proportional to,

$$\Gamma_A \propto D^2 f \lambda_{\text{span}} R \quad 1.$$

where R is the resolving power and λ_{span} the instantaneous wavelength coverage of the spectrograph. Note that this is only a gross simplification of reality for many reasons, since this would imply that one should always push for the largest resolving power and wavelength coverage. First of all, λ_{span} and R are generally not independent from each other due to the limited detector space. Also, the throughput f of a spectrograph typically decreases with increasing R , which depends on its instrumental design, level of atmospheric turbulence, and the presence and performance of a possible adaptive-optics system. A higher R generally makes telluric line removal (Section 2.6) more effective, and a minimum R is needed to measure certain physical characteristics, such as thermal line broadening, spin rotation, or planet orbital velocity. In addition, a higher R means that lines are less blended, increasing the overall HRS signal. A higher resolving power also means that possible stellar effects, such as center-to-limb variations and Doppler shadow can be disentangled from the planet signal more easily. On the other hand, for a certain R the planet lines will start to be resolved, above which the detection speed will no longer increase. In reality, some wavelength regions will be richer in spectral features than others, depending on the type of planet. This will influence the effect of λ_{span} on the detection speed.

In Case B, the target spectrum consists of effectively one single, infinitely narrow line, e.g. exospheric helium, H α . This requires only a very limited instantaneous wavelength coverage (as will also be the case for molecular oxygen in future reflected light studies). In this case the detection speed is proportional to

$$\Gamma_B \propto D^2 f R \quad 2.$$

In Case C we consider high-contrast spectroscopy for which the residual seeing-halo of the host star is the dominant source of noise. Under such circumstances, the detection speed is proportional to,

$$\Gamma_C \propto D^4 f \lambda_{\text{span}} R \quad 3.$$

This depends on the telescope diameter D to the fourth power, because a change in D influences the size of the seeing disk in terms angular resolution elements. In reality, however, this also critically depends on the performance of the adaptive optics (AO) system, the angular distance of the planet to the star in λ/D , and possible sky background and instrumental noise contributions.

Optical high-resolution spectrographs have almost exclusively been designed for RV measurements that require extreme wavelength stability at sub-meter-per-second precision over multi-year timescales. This is often achieved with a combination of light-scrambling, a fibre feed, temperature/pressure stability, and simultaneous wavelength calibration. Since atmospheric signals are generally too weak to measure planet radial velocity at accuracies <100 m/s, such wavelength precision may be considered unnecessary. However, a very stable spectrograph with minimal instrumental artefacts does significantly help in removing telluric and systematic effects, but may negatively affect its throughput.

Several teams are developing instrumentation specifically aimed at combining high-resolution spectroscopy with high-contrast imaging, such as the Keck Planet Imager and Characteriser (KPIC) that combines starlight suppression using Keck's AO system and single-mode fibres transporting the light to the upgraded NIRSPEC with a spectral resolving

power of $R=35,000$ (Mawet et al. 2016, Delorme et al. 2021). Similar instrument designs are chosen for VLT/HiRISE (Vigan et al. 2024) and RISTRETTO (Chazelas et al. 2020), and Subaru/REACH (Kotani et al. 2020). Interestingly, due to a reduced coupling in single-mode fibres, stellar flux is suppressed relative to that of the planet, a mechanism that is also utilised in the GRAVITY instrument at the VLT Interferometer (GRAVITY Collaboration et al. 2020).

Table 1 shows high-resolution spectrographs that are currently most frequently used for exoplanet atmospheric observations, and those that are in the planning for the upcoming ELTs. Fig. 2 shows their detection speed for the different cases. Since Γ scales with D^{2-4} , the instruments on the largest telescopes are generally more powerful. Since optical high-resolution spectrographs have similar instantaneous wavelength coverages, spectrographs on 8-10m class telescopes are typically 4-6 \times faster than those on 4m-class telescopes (1 transit on a larger telescope equals 4 to 6 transits on a smaller one). In the near-infrared wavelength regime, this is true for some instruments on smaller telescopes (such as CARMENES, SPIRou, GIANO and NIRPS) partly compensated by their larger λ_{span} (Case A) and high throughput.

The planned high-resolution spectrographs on future extremely large telescopes will be particularly powerful for *Case C*, since the detection speed scales roughly with D^4 , e.g. making METIS on the ELT almost 300 \times faster than CRIRES+, and ANDES at the ELT and MODHIS on the TMT more than a thousand times. Do note, however, that for the comparison of all these instruments it is assumed that throughput and adaptive optics performances are the same, which will be a challenge.

2.2. Observation and data analysis strategies

Here we explain how HRS observations are typically performed, and discuss procedures for data analyses. For transmission and phase curve observations we review signal-search techniques, and for the former how stellar surface effects like the Doppler shadow and center-to-limb variations can influence observations and need to be accounted for.

2.2.1. Transmission and phase curve observations. A vital feature of time-differential HRS observations is their sensitivity to changes in Doppler-shift of the planet spectrum as function of orbital phase, as shown in Figure 3. The radial component of the planet orbital velocity can vary by tens of km sec^{-1} over a night’s observations. Planet lines therefore rapidly change position relative to the much stronger stellar and telluric features. This means that the latter can be removed efficiently with a minimal impact on the planet signal. For this to work best, instrumental stability is key. Therefore, most observations consist of a continuous series of exposures where possible calibrators are only invoked before and/or after the main observing sequence. Secondary eclipses are generally avoided since no exoplanet signal is present during these times and planet-free spectra are often not needed for calibration purposes. HRS phase curve observations are therefore also well feasible for non-transiting planets.

When planning observations, one should avoid individual exposures that are too long such that planet signals get spectrally blurred. E.g., a planet in a circular 1-day orbit around a solar-type star has an orbital velocity of $\sim 200 \text{ km sec}^{-1}$, with a change in the observed radial component of up to 1 km sec^{-1} per minute. While up to now most HRS transit and phase curve observations are limited to hot Jupiters with fast-changing Doppler shifts,

Table 1 High resolution spectrographs, currently most used or in planning. Columns from left to right show the telescope, its primary mirror diameter, name of the spectrograph, entrance type (slit or fibre), resolving power, wavelength regime, its instantaneous wavelength coverage expressed as $\lambda_{\text{span}}/\lambda$, and whether an adaptive optics system is present or not. The last three columns show the detection speed relative to ESPRESSO and CRIRES+ on ESO’s VLT for the different cases, assuming identical throughput and AO performance, as explained in the main text and presented in Figure 2.

Telescope (m)	Spectrograph (fibre or slit)	R	$\lambda_{\text{min}} - \lambda_{\text{max}}$	$\frac{\lambda_{\text{span}}}{\lambda}$	AO	Detection Speed		
						A	B	C
<i>Optical</i>								
VLT (8.2)	ESPRESSO (f)	140k	0.38–0.79	0.70	–	1	1	
	UVES (s)	100k	0.30–1.10	0.64	–	0.7	0.7	
Keck (10)	HIRES (s)	70k	0.30–1.00	0.70	–	0.8	0.8	
LBT (2x8.4)	PEPSI (f)	130k	0.38–0.91	0.30	–	0.8	2.0	
Gemini (8.1)	MAROON-X (f)	80k	0.50–0.90	0.57	–	0.5	0.6	
Subaru (8.2)	HDS (s)	45k	0.30–1.00	0.50	–	0.2	0.3	
DCT (4.3)	EXPRES (f)	150k	0.38–0.68	0.57	–	0.2	0.3	
ESO (3.6)	HARPS (f)	120k	0.38–0.69	0.58	–	0.1	0.2	
CFHT (3.5)	ESPaDOaS (f)	81k	0.37–1.05	0.96	–	0.1	0.1	
Calar A. (3.5)	CARMENES (f)	95k	0.52–0.96	0.59	–	0.1	0.1	
TNG (3.6)	HARPS-N (f)	120k	0.38–0.68	0.58	–	0.1	0.2	
ELT (39)	ANDES (f)	100k	0.40–1.00	0.86	+	20	16	449
GMT (25)	G-CLEF (f)	100k	0.35–0.90	0.88	–	9	7	
<i>Near-Infrared</i>								
VLT (8.2)	CRIRES+ (s)	100k	0.95–5.30	0.14	+	1	1	1
Keck (10)	NIRSPEC (s)	35k	0.95–5.50	0.11	+	0.3	0.4	0.5
Gemini (8.1)	IGRINS (s)	45k	1.45–2.50	0.53	–	1.8	0.5	
Calar A. (3.5)	CARMENES (f)	80k	0.96–1.71	0.56	–	0.6	0.2	
ESO(3.6)	NIRPS (f)	82k	0.95–1.80	0.62	–	0.7	0.1	
CFHT(3.5)	Spirou (f)	75k	0.95–2.35	0.85	–	0.9	0.1	
TNG (3.6)	GIANO (f)	50k	0.90–2.50	0.94	–	0.7	0.1	
ELT (39)	ANDES (f)	100k	1.00–1.80	0.57	+	100	25	2264
TMT (30)	MODHIS (f)	100k	0.95–2.40	0.87	+	90	15	1210
GMT (25)	GMTNIRS (f)	50k	1.07–2.45	0.78	+	37	6	340
<i>Mid-Infrared</i>								
VLT (8.2)	CRIRES+ (s)	100k	0.95–5.30	0.14	+	1	1	1
Keck (10)	NIRSPEC (s)	25k	0.95–5.50	0.11	+	0.3	0.4	0.5
ELT (39)	METIS (s)	100k	3.00–5.00	0.07	+	12	25	278
GMT (25)	GMTNIRS (f)	100k	2.90–5.30	0.59	+	36	9	336

planets in wider orbits and/or around lower-mass stars have significantly lower orbital velocities, causing the change in Doppler shift to be insufficient to be utilised for telluric and spectral line removal. However, successful HRS phase-curve observations near quadrature, and transit measurements on relatively broad spectral features, indicate that HRS spectroscopy is also possible under these circumstances using other calibration methods, e.g. by comparing in and out of transit data (Cheverall & Madhusudhan 2024), or spectra taken at very different phases.

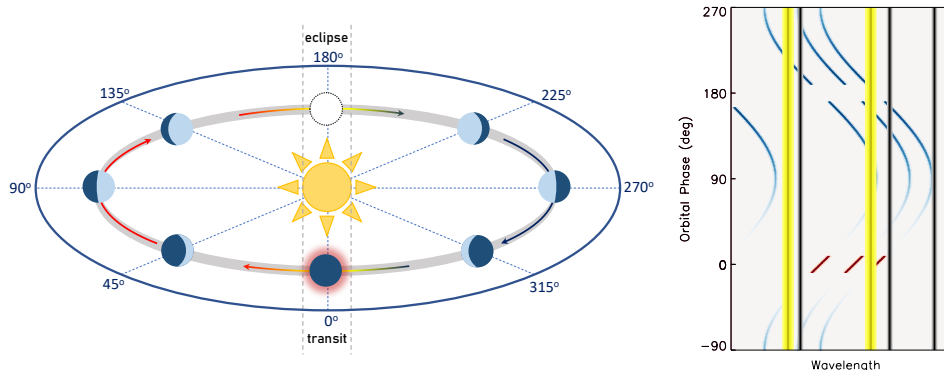


Figure 3

Appearance of a planet as function of orbital phase (left). If in a near edge-on orbit the system will exhibit transits, allowing transmission spectroscopy, and eclipses - when the planet is blocked from view. The diagram on the right shows how in an observing sequence telluric (black) and stellar (yellow) lines are quasi static in wavelength, while those features originating from the planet (dayside emission in blue, transmission in red) exhibit strong Doppler effects.

2.2.1.1. Analysis of transmission and phase-curve data. The first important element of the data analysis of transmission and phase-curve data is the removal of the stellar and telluric contaminations. The telescope and instrument throughput generally varies with time and wavelength, e.g. due to seeing and airmass effects, which are impossible to calibrate accurately. To mitigate this, spectra are normalised and often high-pass filtered such that any broadband information is lost. To first order, the stellar lines do not vary in strength and position with time, meaning that removal of the mean spectrum will take care of the stellar contribution. While the telluric line positions are quasi-stable with time, the line strengths vary due to changes in airmass and possible changes in the observatory's atmospheric circumstances. To first order, these variations are similar for all tellurics and therefore can be measured in some strong lines and applied to all others. If needed, such correction can be performed for different telluric species, e.g. water and methane, separately.

For high signal-to-noise data, however, there are more subtle issues. The wavelength solution of the instrument may vary over time, or Earth-atmospheric winds may change the exact wavelength position of telluric lines. Seeing effects may change the spectral resolution for slit spectrographs. Stellar lines move due to the Earth's rotation and gravitational pull of the planet overnight, and may change in shape and strength due to stellar activity. Instead of aiming to model all these different effects, a blind search for systematic effects in the data can be achieved using principle component analysis. Currently, one of the most popular algorithm is SysRem (Tamuz et al. 2005), originally developed to detrend lightcurves of transit surveys. SysRem and other algorithms that are being used to remove telluric and stellar contamination, all will affect and remove part of the target planet spectrum, an effect that ideally needs to be taken into account e.g. by analysing artificial injection signals (see below). In future analyses, it may be possible to simultaneously forward model and retrieve the stellar spectrum, telluric contamination, instrumental effects and the planet spectrum without losses. Such approach is already being implemented in high-contrast spectroscopy (Ruffio et al. 2019) for which the ratio of planet signal to the various noise contributions is

significantly more favourable.

2.2.1.2. Cross-correlation, signal-search techniques, and detection significance.

The procedure to remove telluric and stellar features as described above will largely preserve the line-features in planetary spectra because of the change in Doppler shift of the planet over the observing sequence. Except for single-line analyses, the next step is to optimally combine the signals from different lines in the spectra, with each individual line still buried in the noise. This is often done by cross-correlating the residual spectra with a model template (see for a detailed description the review by Birkby 2018). The more similar the model template is to the planet spectra, the higher the cross-correlation signals will be. In the ideal case, the cross-correlation signal of a spectrum with N well-separated, equally strong lines will boost the signal-to-noise by a factor of \sqrt{N} compared to that of one individual line. Alternative methods exist to extract the total planet signal, such as techniques using Doppler tomography (Watson et al. 2019, Matthews et al. 2024b), and log-likelihood methods that directly compare model templates with the data (Gibson et al. 2020).

In the case of direct fitting of template models to spectra, the change in planet Doppler shift as a function of time can be included as extra free parameters. Assuming circular orbits, and assuming that the orbital period and time of inferior conjunction are known, the radial velocity of the planet depends on the RV amplitude, K_p , and the system velocity, V_{sys} , where the former is governed by the stellar mass and orbital inclination. In the case of combining cross-correlation signals, these are often calculated, Doppler shifted, and added, for a wide range of (K_p, V_{sys}) combinations to produce a so called K_p - V_{sys} diagram. This has the added benefit that such a diagram provides an independent estimate of the significance and reliability of any detected signal by showing the cross-correlation noise properties in regions of the K_p - V_{sys} diagram where no signal is expected (see below). Note that atmospheric circulation patterns such as day-to-nightside winds may alter the exact K_p and V_{sys} of the planet signal. Non-circular orbits make the K_p, V_{sys} diagram less intuitive (e.g. Grasser et al. 2024).

The data points in a $K_p - V_{sys}$ diagram are not independent from each other. Figure 4 shows such diagram for a noiseless time-series of cross-correlation signals (left panel) of a hypothetical hot Jupiter and the corresponding $K_p - V_{sys}$ diagram (right panel). A signal from any single observation can in principle be fitted with a linear combination K_p and V_{sys} . For this reason, observations taken over a relatively short orbital phase range result in characteristic patterns as seen in the right panel of Fig. 4, with a typical X-shape if observations are combined from both before and after the secondary eclipse.

The $K_p - V_{sys}$ diagram is often used to estimate the statistical significance and reliability of an observed signal by comparing it to the noise properties in this diagram away from the expected K_p and V_{sys} . One should be careful that the noise properties are a function of K_p , since the lower the K_p , the smaller the change in radial velocity during the observing sequence and the more PCA algorithms will both remove the noise and any planet signal. For strong signals, aliasing may affect noise estimates. Alternatively, the Welch T-test can be used on the cross-correlation data by comparing the distribution of cross-correlation (CC) values inside and outside the expected radial-velocity trail (e.g. as shown in the left panel of Fig. 4). One should take into account that neighbouring CC values may not be independent of each other and that the properties of the CC-noise may not be Gaussian, two basic assumptions of the Welch T-test.

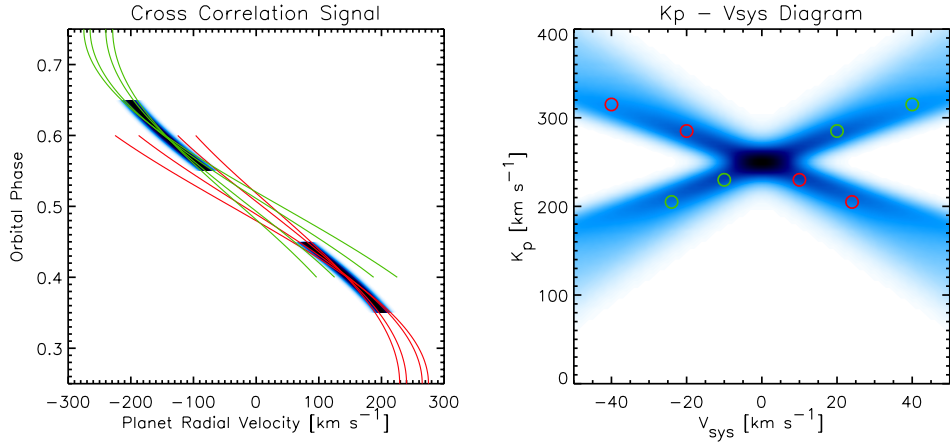


Figure 4

The left panel shows a simulation of a cross-correlation signal (in blue-black) of a hot Jupiter observed over two orbital phase ranges, before ($\phi \sim 0.4$) and after ($\phi \sim 0.6$) secondary eclipse. The right panel shows the resulting $K_p - V_{\text{sys}}$ diagram with its characteristic X-shaped appearance. The origin of this X-shape comes from the range of (K_p, V_{sys}) combinations that fit either the pre-eclipse or post-eclipse part. This is shown by the red and green orbital solutions in the left panel, which correspond to the (K_p, V_{sys}) combinations indicated by the red and green circles in the diagram on the right.

HRS observers often make use of artificially injected signals. They can make sure that the different elements of the analysis pipeline work properly, they can help to assess the quality of the observed data throughout the night and/or over multiple nights and identify in which Echelle spectral orders specific molecules exhibit the strongest signals or where (residual) tellurics increase the local noise.

2.2.1.3. RM Effect, Doppler Shadow, and CLV. In the case that HRS observers pursue a transmission spectrum with exoplanet atmospheric lines that are also present in the photosphere of its host star, the subsequent data analysis is prone to become significantly more complicated. Examples are alkali metals such as sodium in Hot Jupiters, and metal lines in Ultra-Hot Jupiters (UHJ, $T_{\text{eff}} > 2000$ K). As a consequence, two effects may interfere with the planet transmission spectrum: the planet Doppler shadow and stellar center-to-limb variations (CLV).

The Doppler shadow is inherently the same as the Rossiter-McLaughlin (RM) effect and constitutes a temporal deformation of rotationally-broadened stellar line profiles during transit. The occulted part of the stellar surface momentarily does not contribute to the overall stellar spectrum, leaving a 'shadow' in the rotationally-broadened lines. In the course of a transit, this shadow moves from the blue to the red wing of a stellar line, depending on the spin-orbit angle and the transit impact parameter. The effective strength of the shadow depends on the opacity of the stellar line and the size of the planet. The Doppler shadow, which has a sign that is opposite to any exoplanet transmission signature, has to be modelled and removed from the data so not to bias the results. In most systems the transmission signal and Doppler shadow cross-over in velocity at some point during transit.

At such a moment in time, the effective size of the planet is larger due to the additional absorption in its atmosphere, increasing the strength of the shadow making it very hard to disentangle the two effects. Data from such an epoch are therefore often masked.

Center-to-limb variations (CLV) are also an important effect (Czesla et al. 2015, Yan et al. 2017). The local spectrum near the stellar limb is significantly different from that near the centre of the stellar disk due to the different angle of incidence. It means that near the beginning or end of a planet transit, the spectrum of the occulted stellar surface can be significantly different from the average spectrum and could be falsely attributed to a planet transmission signal.

In contrast to CLV, whose effects can be modelled and removed, other stellar surface inhomogeneities are more challenging. A planet's path over the stellar surface may cross more or fewer star spots, i.e. the occulted stellar surface may have on average a different effective temperature than the unocculted stellar surface. Such effects currently plague JWST transmission spectroscopy of planets around cool dwarf stars, unable to differentiate between atmospheric transmission features and stellar surface effects (e.g. for water; Moran et al. 2023). HRS observations could potentially help to distinguish between the two, because the radial velocity of the occulted stellar surface is mostly different from that of the planet - although effects are small.

2.2.2. High-contrast spectroscopy. High-contrast HRS relies on a telescope with an adaptive optics (AO) system and optionally a coronagraph, from which light can be fed to a high-resolution spectrograph. Only in the special cases for which the planet is sufficiently far away from its host star, is no AO-system required. In the case of planet thermal emission, the planet spectrum is in most cases significantly different from that of the star, because the effective temperature of the planet is much lower. In the case of scattered light, the planet and star spectrum are quasi-identical, but the reflected light spectrum for the planet will be Doppler shifted for most orbital phases. Therefore, in both cases, planet light can be spatially as well as spectroscopically separated from that of the star, and many studies have identified high-resolution spectroscopy in combination with high-contrast imaging as a potentially powerful method to find new planets and characterise them (e.g. Sparks & Ford 2002, Riaud & Schneider 2007, Kawahara & Hirano 2014, Snellen et al. 2015).

Blind searches for extrasolar planets with unknown positions require a form of integral field spectroscopy, which is currently only available at moderate spectral resolution (such as OSIRIS on the Keck Telescope, and ERIS and MUSE on ESO's VLT). In the case of a slit or fibre spectrograph, the planet position relative to that of the star must be known at the time of observation. If the host star is positioned on the detector and no coronagraph is present, exposure times are generally short to avoid saturation, meaning that the fainter planet spectrum could be degraded by instrumental read-out noise. On the other hand, the inclusion of a bright star spectrum can be beneficial for the data analysis.

The observed spectrum at the planet position generally contains flux from the star and planet, both modified by telluric absorption, and possibly a sky background contribution. The latter can be effectively removed by moving the target along the slit or IFU in between exposures. To first order, the stellar contribution (including tellurics) at the planet position will only slowly vary with wavelength, allowing it to be scaled and removed or included in the forward modelling, with the observed star spectrum as a concurrent reference. The residual spectrum can subsequently be searched for planet molecular signatures using cross correlation techniques as for transit and phase-curve observations. However, a particularly

high data-quality requires more complex data analyses. E.g. in the case of slit-spectroscopy a combination of good seeing and AO performance can cause the effective size of the star to be smaller than the slit-width. This can cause the planet-spectrum and associated telluric absorption to have a higher spectral resolution than the star-spectrum with associated tellurics. Also, the wavelength solution may vary along the slit. Effective strategies for the removal of the stellar and telluric contributions need to take this into account and will depend on the particular atmospheric circumstances and planetary system. E.g., these can include radiative transfer modelling of telluric absorption and a set of principal components of the residuals to include systematic effects (Ruffio et al. 2023). Ideally, the stellar, planet, telluric contributions and resolution effects should be simultaneously modelled to retrieve reliable and unbiased atmospheric parameters and their uncertainties, but this is beyond current methods and computer capabilities.

2.3. Atmospheric modelling

Atmospheric modelling is an integral part of HRS observations. Model templates are used to tease out planetary signals, but also for atmospheric retrieval studies. Any HRS observation can only be as good as the models used. Equally important: any model is only as good as its underlying opacity data. Small errors in line positions can already lead to significant losses in signal. Therefore line positions need to be accurate to a fraction of the spectral resolving power. Another challenge is the line strengths, which become increasingly difficult to calculate and measure in laboratory settings at higher temperatures. Pressure broadening calculations may also be relevant, in particular for thermal emission spectra. Here we discuss the origin of opacity data, common software packages for radiative transfer calculations, and review the art of atmospheric retrievals.

2.3.1. Atomic and molecular opacity data. Accurate line data for atomic and ionic species are mostly readily available from databases such as from the National Institute of Standards and Technology (NIST¹) and the Vienna Atomic Line Database (VALT²). However, the spectra of polyatomic molecules are extremely complex with potentially up to billions of transitions playing a role. While a proper discussion of the challenging practicalities of generating molecular line lists is beyond the scope of this review, this is a complex industry that deserves more attention. E.g. it took a significant part of a quantum-chemistry PhD project to calculate the line data for phosphine up to $T=1500$ K (Sousa-Silva et al. 2015). In addition to accurate line position, line broadening calculations can also be important for retrieval analyses.

A leading supplier of molecular line data at high temperatures is the ExoMol Group, working with the concept of *first principles theory informed by experiment* (Tennyson & Yurchenko 2021). ExoMol now validates and adjusts line energies depending on laboratory measurements, leading to very high accuracy line lists. Its database contains line lists for more than 80 molecules, often including isotopic variants. High temperature line lists have also been produced by the TheoRets project (Rey et al. 2016), MoLLIST (Bernath 2020), and by NASA Ames. The HITRAN database (Gordon et al. 2017) provides line data applicable at low temperatures for several dozens of small molecules present in the Earth

¹<https://www.nist.gov/pml/atomic-spectra-database>

²<https://vald.astro.uu.se/>

atmosphere, and expanded to higher temperatures in HITEMP (Hargreaves et al. 2020). If the line data are insufficiently accurate or incomplete it can significantly hamper the detection of molecules, such as shown by Hoeijmakers et al. (2015) for the case of TiO and de Regt et al. (2022) for VO. The optical spectra of both these molecules are particularly challenging as they are dominated by electronic transitions, but significantly improved line data have become available since (McKemmish et al. 2019, Bowesman et al. 2024).

2.3.2. Radiative transfer calculations. Radiation transfer calculations are needed to produce model exoplanet emission and transmission spectra. An example of an easy-to-use publicly available python package for this purpose is petitRADTRANS (Mollière et al. 2019), but there are many alternatives such as HELIOS (Malik et al. 2017), EXo-REM (Baudino et al. 2015), NEMESIS (Irwin et al. 2008), HyDRA (Gandhi & Madhusudhan 2018), CHIMERA (Line et al. 2014), PLATON (Zhang et al. 2019), and others. These codes typically require pre-computed opacity grids of relevant atoms, ions and/or molecules as function of pressure and temperature, in addition to continuum opacity sources such as $\text{H}_2 - \text{H}_2$, $\text{H}_2 - \text{He}$ collision-induced absorption and H^- . Most radiative transfer codes have also a way to include the effects of clouds, either physically motivated (e.g. MgSiO_3 , Fe, etc.) or simple grey cloud models, controlled by parameters such as the atmospheric pressure and opacity at the cloud base, and a power law index that sets the decay towards lower pressures.

For the calculation of transmission spectra, in its basic form, the planet atmospheric structure is assumed to be independent of longitude or latitude, and the assumed pressure-temperature profile and surface gravity (e.g. at 1 bar) is converted to a radius-temperature relation and parameterised as a set of layers, each with a specific pressure and temperature. The optical depth for a ray of light grazing the atmosphere is determined as a function of impact parameter, and subsequently converted into a transmission spectrum. For the calculation of planet emission spectra, similar set-ups are used for calculating the transmission of each layer, using a range of angles between the direction of the light rays and the atmospheric normal to determine the average emission from the planet disk. Since the full radiative transfer solution is a scattering atmosphere is computationally slow, it is often assumed that the scattering is weak compared to the absorption.

2.3.3. Retrievals of atmospheric parameters. The aim of atmospheric retrievals is to determine atmospheric properties and their uncertainties from an observed spectrum. In the context of exoplanets, this was first pioneered by Madhusudhan & Seager (2009), forward modelling millions of (low resolution) spectra for a ten-dimensional grid of input parameters. Subsequently, for all these model spectra it was determined whether they, within uncertainties, fit the observed data to derive the atmospheric properties.

Atmospheric retrievals for HRS are challenging for several reasons. In the case of HRS transit and phase-curve spectroscopy the observed spectrum is modified by the data reduction processes, such as PCA and filtering techniques. The forward models need to go through similar data processing to allow for a reliable comparison with the data. Furthermore, HRS data volumes can be enormous with up to tens of thousands of pixels per individual spectrum. Brogi & Line (2019) presented a Bayesian atmospheric retrieval framework applicable to HRS observations, for which they developed a mapping from cross-correlation to log-likelihood. Gibson et al. (2020) subsequently introduced a framework that directly computes the likelihood of a model fit to observations. Monte Carlo Markov Chains (MCMC)

and Nested Sampling techniques can then be employed to explore parameter space. Fisher et al. (2020) have presented a random forest supervised machine learning technique to perform the retrievals. Ruffio et al. (2019) pioneered an approach in which the signal is forward modelled in such a way that pre-processing of the data (such as cross-correlation and data interpolation) is minimised, preserving the statistical properties of the data as much as possible and therefore the likelihood accuracy.

A key aspect of atmospheric retrievals is the choice of assumptions for chemical modelling and parameterisation of the atmospheric temperature structure. When chemical equilibrium is assumed, chemical abundances vary as function of altitude and strictly depend on temperature, pressure, metallicity and atomic ratios such as C/O, while disequilibrium processes such as photochemistry or rain-out condensation are ignored. Since vertical mixing time scales can be significantly shorter than those to reach chemical equilibrium, in particular at low pressures, a quench pressure can be introduced (Zahnle & Marley 2014). Below this pressure, higher up in the atmosphere, the chemical abundances are assumed to be governed by chemical equilibrium at the quench pressure because vertical mixing dominates. E.g. in some hot Jupiters the temperature at mbar pressures is low enough that significant methane would form if the atmosphere would be in chemical equilibrium. However, the gas largely originates from deeper atmospheric layers with higher temperatures and does not have time to adjust to the local circumstances (Cooper & Showman 2006). An alternative assumption is to adopt *free chemistry* without any restrictions on volume mixing ratios except that they are constant as function of altitude. The abundance of every absorber is then a free, independent parameter. If the quality of the data allows, it can be very informative to compare outcomes of different retrieval set-ups to address the validity of chosen assumptions.

Also the atmospheric temperature-pressure profile can be parameterised in many ways, from a complete free format, to largely physics-informed T/p profiles (e.g. Guillot 2010). A choice will also have to be made whether to include clouds (physically motivated or grey) in the retrievals or not. If an opaque cloud layer is present, but clouds are not included in the retrieval set-up, the retrieved T/p profile may get deformed. E.g. since in such case no flux is coming from below the cloud layer, this can be mimicked by an isothermal profile (Burningham et al. 2017).

2.4. Potential pitfalls

HRS can be a very complex technique, both in terms of observations and data analysis. Here a non-exhaustive list of potential pitfalls is discussed for those HRS users new in the field.

1. Exposure time blending When planning transit or phase curve spectroscopic observations, individual exposure times should not be set too long to avoid spectral blending. The change in the radial velocity of the planet may be so large during the exposure that it affects the effective resolving power of the observations.

2. Overlap of transmission signal with Doppler shadow For some transiting systems, the trail of the Doppler shadow largely overlaps with that of the planet transmission signal. This means that at any moment during transit, the radial component of the orbital velocity of the planet matches the radial velocity of the occulted stellar surface, making analyses of

planet transmission features that are also present in the stellar photosphere very challenging. Notable examples are HD 209458 b and MASCARA 1 b.

3. *Velocity broadening of scattered light signals* When probing starlight reflected off atmospheres of short-period planets, one has to take into consideration that reflected signals can be significantly velocity broadened (e.g. Spring et al. 2022). While the spin-velocity of the host star may be very slow, in the rest frame of the planet it will make about one revolution per orbital period, making detection of scattered light more challenging. Since in the tau Bootis system both star and planet are tidally locked, the scattered stellar lines are ‘unbroadened’ and expected to be significantly more narrow than those in the direct stellar spectrum, making it a popular target for reflected light studies (Charbonneau et al. 1999, Collier Cameron et al. 1999, Hoeijmakers et al. 2018b), but the planet turned out to be very dark.

4. *Conversion of signal-to-noise to statistical significance* The signal-to-noise ratio of a measurement can be converted into a statistical significance by assuming a Gaussian noise distribution. Since in this case a signal at $S/n=3$ corresponds to a 0.3% probability that it is caused by a random noise fluctuation, this could in principle be considered as a firm detection. However, the fact that to arrive at such detection many post processing choices have been made should not be overlooked; how to extract the spectra and remove the telluric and stellar absorption lines, which spectral model to choose to perform the cross-correlation, and freedom in the exact location of the signal in the (K_p, V_{sys}) diagram due to a priori unknown atmospheric winds effects. Also, overall it can be difficult to assess to what extent the noise distribution is indeed Gaussian. These effects make the probability that a spurious signal is seen at $S/n=3$ significantly higher than 0.3%. Therefore, many studies use a threshold of $S/n=4$ or 5 to claim a detection, which still may not be sufficient. Even more conservative is to require a detection in multiple transits or phase curve observations.

5. *Accidental fabrication of fake signals* For many HRS measurements, data over multiple nights and/or many spectral orders have to be combined. This is often done by deriving the CC functions per order and night which are subsequently combined using optimal weights. These weights can be important because the data quality may be different from one night over the other, and a specific molecule may only have significant opacity in certain spectral orders of the spectrograph. It is of utmost importance that the calculation of these weights is purely based on injected signals and not on the observed data. Otherwise the analysis may result in a fake, fabricated signal (see for a discussion; Cabot et al. 2019). A modern high-dispersion spectrograph, for example, can have 80 spectral orders. If there is no planetary signal at all, and the resulting cross-correlations from the individual orders contain all pure uncorrelated Gaussian noise, still $\sim 16\%$ and $\sim 2.5\%$ of the orders will exhibit a 1σ and 2σ CC-peak respectively, which with optimal weights will combine into a completely spurious signal of $\sim 6\sigma$. Note that the contribution from the signal injection to the cross-correlation function needs to be separated from that of the observed spectrum, otherwise the latter is still prone to bias the determination of the optimal weights (Cheverall et al. 2023).

Also, the number of PCA or SysRem components, required to remove the telluric and stellar features in the spectra, needs to be chosen, which may also depend on the observing night and spectral order (e.g. depending on the strength of the telluric features). These

need to be treated in the same way.

6. Unrealistic and biased uncertainties in retrieved parameters Results from atmospheric retrieval analyses are mostly not free from biases and can provide unrealistically small uncertainties. This can have several reasons which are important to investigate. Different data sets, i.e. with different wavelength regimes, spectroscopic resolving power, or S/n levels, can result in retrieval results that are significantly different from each other. First of all, it is generally assumed that spectral data points and their uncertainties are independent of each other, which is often not the case, e.g. due to model inaccuracies or errors in telluric removal. The atmospheric temperature structure (and abundance profiles), i.e. can be parameterised in many ways, possibly none providing the perfect solution and therefore all resulting in their own biases. One way to characterise the strength and scale-length of correlated noise is using Gaussian Processes and include them in the retrieval set-up (Kawahara et al. 2022). In addition, uncertainties from pre-processing are mostly not included, such as small errors in the flux calibration from a spectroscopic standard star that result in inaccuracies in the spectral slope. These can be included by adding extra order-normalisation parameters, spectral slope parameters, or by removing any low-frequency spectral information (by high-pass filtering) altogether.

Another important source of unrealistically small uncertainties is the inclusion of too few free parameters in the retrievals. The Bayesian Information Criterion (BIC) is widely used to assess whether extra parameters provide a significantly better fit. If not, such extra parameters are not included in the retrieval. However, even if extra parameters do not result in a better fit, they may still influence the uncertainty (and best-fit value) of other parameters. For example, for an observed spectrum with relatively low S/n, retrievals may suggest that there is no statistical evidence for any deviation from chemical equilibrium, or for the presence of clouds. However, performing a retrieval with free-chemistry and with including the possibility of clouds, or 3D effects, can significantly change the outcome and enlarge the uncertainties on retrieved abundances. Sometimes strict assumptions are chosen, because the data would otherwise not provide meaningful constraints.

3. Results on close-in exoplanets

In this section, literature results on HRS atmospheric characterisation of close-in exoplanets, mostly hot Jupiters, are summarised and discussed. In such a vibrant field of research as exoplanet characterisation it is impossible to provide a complete overview of all the work presented in the literature, in particular because during writing new studies appeared on an almost daily basis. We review observations of specific atmospheric species, constraints on temperature structure, atmospheric dynamics and outflows, reflected light searches, and chromatic Doppler-shadow measurements.

3.1. Measurements of atoms, ions, and molecules

Sodium H & K lines Sodium was predicted to produce the strongest features in optical transmission spectra of Hot Jupiters (Seager & Sasselov 2000) and was the first chemical element detected in an exoplanet atmosphere, in HD 209458 b using the HST (Charbonneau et al. 2002). Studying sodium in transmission is challenging because stellar sodium lines are very strong, in particular for G and K-type stars. This means that the signal-to-noise of a

planetary sodium signal at mid-transit is generally low and Doppler-shadow and CLV effects are particularly strong. While Snellen et al. (2008) confirmed the original HST detection of sodium with Subaru, Casasayas-Barris et al. (2021) find no evidence for sodium at this level in superior ESPRESSO observations taken more than a decade later. For this system, the radial velocity trail of the planet almost overlaps with the Doppler shadow, making the analysis of this target particularly difficult. In the earlier studies, CLV effects were not taken into account, so at least part of the original sodium signal could be attributed to this. On the other hand, due to the overlap of the RV-trail and Doppler shadow, the RM effect at sodium wavelengths is stronger in the case of a planetary atmospheric contribution, counteracting a transmission signal (see Carteret et al. 2024, for a recent discussion). Alternatively, long-term variability (i.e. due to changes in cloud-coverage in the terminator region) could play a role, although temporal variability can too easily be invoked to explain differences between data sets.

The left panel of Figure 5 provides an overview of the currently known population of transiting Hot Jupiters around bright stars ($V < 13.5$) available in the NASA Exoplanet Archive³. Plotted are their equilibrium temperature, T_{eq} , versus what we define as the Scale Height Contrast (SHC). The latter is the expected transmission signal from an opaque atmospheric ring with a thickness of one scale height, H , corresponding to

$$SHC = (2\pi R_p H) / (\pi R_s^2)$$

where R_p and R_s are the planet and host star radius respectively. It is a first-order measure of how strong a transmission signal is expected to be. The thick circles indicate those Hot Jupiters that have an HRS sodium detection presented in the literature, where the colour is an indication of T_{eq} . HRS detections exist for hot Jupiters with a wide range of equilibrium temperatures, up to the hottest planets known. This literature sample of planets with sodium detections is likely marred with biases. Also non-detections and their associated upper limits are poorly reported and are not included here. The SHC of those planets with detections is larger than average, probably because mostly promising targets are being observed, and those with a smaller SHC fall below typical detection limits.

The right panel of Figure 5 shows the observed strength of the sodium signals versus SHC. The data, and their origin from the literature, are presented in Supplementary Table 1. This strength is simply taken as the relative depth of the transmission signal, ignoring spectral resolution and intrinsic width of the sodium features. Despite the many caveats regarding sample selection, completeness and other biases, it is interesting to see that the strengths of the sodium signals correlate with SHC. A similar analysis was performed by Langeveld et al. (2022) showing a comparable relation on a smaller sample. The sodium signals in Hot Jupiters extend typically between 20 and 80 scale heights above their continuum absorption. A notable exception is WASP-127 b, which has the largest SHC in the sample but a relatively weak sodium feature (Allart et al. 2020). Assuming that these sodium features dominantly originate from the hydrostatic part of Hot Jupiter atmospheres, the observed planet-to-planet variations could be driven by variations in high-altitude cloud decks, sodium abundance, velocity broadening, and photo-ionisation for planets at the highest temperatures. Alternatively, one could argue that many of the signals are so strong, associated with micro-bar pressure levels, that they likely originate from exospheric outflows (Seidel et al. 2020).

³retrieved on 4/1/2024 from <https://exoplanetarchive.ipac.caltech.edu>

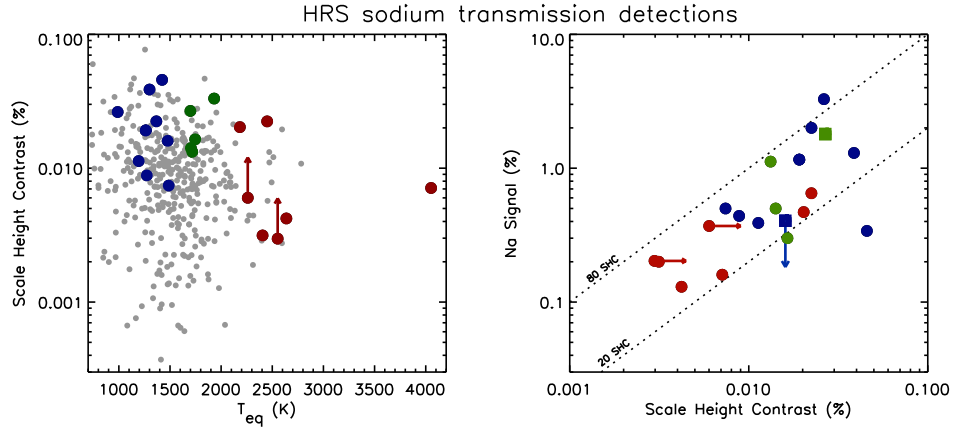


Figure 5

Left panel: Currently known population of transiting Hot Jupiters around bright stars² with orbital periods <10 days, masses $>0.1 M_{\text{Jup}}$, and radii $>0.5 R_{\text{Jup}}$. Their equilibrium temperatures (assuming a zero Bond albedo) are plotted versus Scale Height Contrast (see main text). The coloured symbols (red: $T_{\text{eq}} > 2000$ K; green: $1500 \text{ K} < T_{\text{eq}} < 2000$ K; blue: $T_{\text{eq}} < 1500$ K) are planets with HRS sodium detections presented in the literature. Those with lower limits in their scale height contrast have yet an unknown mass. The signals of the two planets (HD209458 b and WASP-17 b) marked with squared symbols are derived from their integrated light curve, assuming the sodium signal is 0.5 \AA wide. Right panel: Strength of the sodium signal versus Scale Height Contrast. The data, as well as literature references, are provided in Supplementary Table 1.

Other metals and ions Since sodium is so prominent in the optical transmission spectrum of Hot Jupiters, it is the subject of many studies. In particular in Ultra-Hot Jupiters (UHJ), numerous other metals and ions have been detected. Seager & Sasselov (2000) already showed that potassium should also provide observable transmission signals for hot Jupiters. However, observational successes have been limited. While some popular high-resolution spectrographs do not cover the potassium lines, they are at wavelengths hampered by telluric absorption from molecular oxygen. Initial reports of potassium from HST observations (Sing et al. 2015) of WASP-31 b have not been confirmed with HRS (Gibson et al. 2019). Chen et al. (2020b) seems the only reported HRS potassium detection, in WASP-52 b.

At temperatures $T_{\text{eq}} > 2000$ K, optical transmission spectra of gas giant planets are expected to be cloud-free, close to chemical equilibrium, and dominated by features from atomic and ionised metals (Kitzmann et al. 2018). Indeed, HRS has been prolific in detecting such signals in UHJs (Hoeijmakers et al. 2018a, 2019). Figure 6 shows a schematic overview of detections presented in the literature so far in the context of the periodic table, either in neutral or ionised state, including alkali metals (lithium, sodium, potassium), alkaline earth metals (magnesium, calcium, strontium, and barium), and transition metals (scandium, titanium, vanadium, chromium, manganese, iron, cobalt, nickel, yttrium).

It is interesting to discuss those elements that are *not* seen. Most of these have either too low cosmological abundances, are insufficiently spectroscopically active, or have no significant lines in the optical wavelength regime (e.g. Kesseli et al. 2022). Also, condensation on the nightside can play a role, where those elements with a high condensation temperature (refractory elements such as Ti, Al, and Sc) could rain-out on the night side

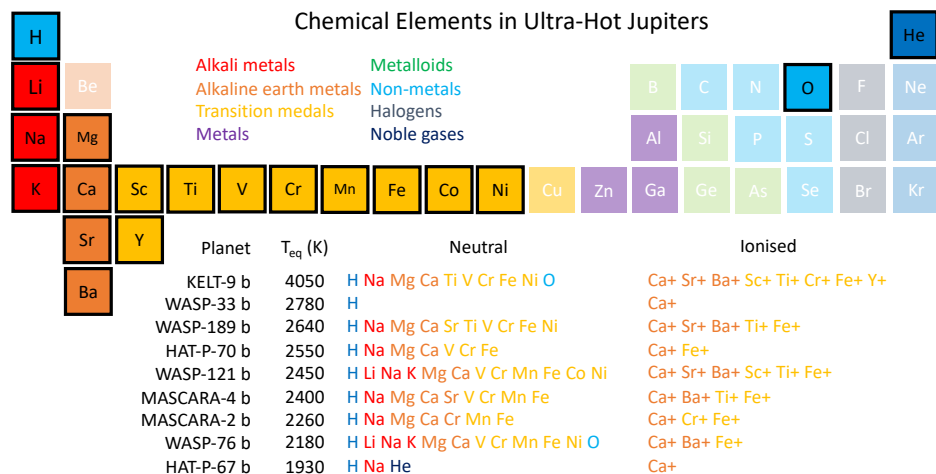


Figure 6

Overview of the chemical elements detected in the transmission spectra of Ultra-Hot Jupiters (UHJ). Planets are ordered by decreasing equilibrium temperature. WASP-33 b is a more challenging target due to the presence of significant stellar pulsations. References: Borsa et al. (2021); Borsato et al. (2023); Hoeijmakers et al. (2018a, 2019, 2020, 2022); Yan & Henning (2018); Cauley et al. (2021); Yan et al. (2019); Prinoth et al. (2024); Prinoth et al. (2023); Stangret et al. (2020, 2022); Bello-Arufe et al. (2022, 2023); Azevedo Silva et al. (2022); Ben-Yami et al. (2020); Merritt et al. (2021); Maguire et al. (2023); Gandhi et al. (2023b); Jiang et al. (2023); Zhang et al. (2022); Casasayas-Barris et al. (2019); Fossati et al. (2023); Nugroho et al. (2020b); Ehrenreich et al. (2020); Taberner et al. (2021); Deibert et al. (2021); Pelletier et al. (2023).

and be "cold-trapped" deep in the atmosphere, preventing them from being mixed back into the upper layers, resulting in low abundances in both dayside and transmission spectra (Hoeijmakers et al. 2022, Pelletier et al. 2023). Titanium is indeed not detected in the three studied UHJs with the lowest equilibrium temperature (Fig. 6). At lower temperatures it is expected that iron will rain out (Kitzmann et al. 2018, Ehrenreich et al. 2020). This is in agreement with non-detections of iron and nickel in HAT-P-67 b in contrast to sodium and ionised calcium (Bello-Arufe et al. 2023).

Ionisation may also play a role in the apparent under-abundance or non-detections of neutral species (Kesseli et al. 2022, Gandhi et al. 2023b). Some metalloids and non-metals have been detected in dayside spectra (Cont et al. 2022b) or locked up in molecules (such as CO; Yan et al. 2023). Detections of chemicals with very high atomic mass have been reported, such as rubidium and samarium (Jiang et al. 2023) in MASCARA-4 b and terbium in KELT-9 b (Borsato et al. 2023). These species have very low cosmic abundances and their presence in UHJ atmospheres needs confirmation.

In recent years, great advances have been made in retrieval studies of exoplanet atmospheres such that abundances can be quantified. UHJs are ideal targets for this purpose due to the expected chemical equilibrium and absence of clouds. Relative chemical abundances are generally much better constrained by transmission spectra than absolute abundances because they are less sensitive to the atmospheric temperature structure and absolute pressures probed. Gibson et al. (2022) retrieves relative abundances for WASP-121 b consistent

with solar values, except magnesium. For WASP-76 b, Pelletier et al. (2023) show seven species to have abundances relative to iron similar to proto-solar (except for those elements that are cold-trapped), while its overall metallicity appears only possibly slightly enriched (at $\sim 1\sigma$) compared to its host star. Gandhi et al. (2023b), in a homogeneous study, retrieves the absolute and relative abundances from the optical transmission spectra of six UHJs. They show that iron abundances agree well with solar values, but that other species exhibit more variations for reasons discussed above. Note that these retrieval studies assume the atmospheres to be in hydrostatic equilibrium, while actually some species may be associated with exospheric outflows (Zhang et al. 2022).

Carbon monoxide, water, and other molecules The first overtone absorption band of CO at $2.3 \mu\text{m}$ is an ideal target for ground-based HRS, due to its strong, well-separated set of lines in a relatively telluric-free part of the spectrum. Detections of CO and H₂O have historically dominated the HRS literature, shown to be present in both the transmission and dayside spectra of the two archetype hot Jupiters HD 209458 b (Snellen et al. 2010, Brogi et al. 2017, Hawker et al. 2018) and HD 189733 b (de Kok et al. 2013, Rodler et al. 2013, Birkby et al. 2013, Brogi et al. 2016). These molecular gases have so far not been widely studied in transmission spectra (Basilicata et al. 2024, Boucher et al. 2023, Maimone et al. 2022, Hood et al. 2024), in contrast to thermal dayside spectra, where they are found in relatively cool planets such as HD 189733 b, 51 Pegasi b, to Ultra-Hot Jupiters (e.g. Birkby et al. 2017, Brogi et al. 2023, Holmberg & Madhusudhan 2022). In the case of non-transiting planets, detection of CO and/or H₂O have lead to the determination of their orbital inclinations, breaking the $\sin i$ degeneracy and solving for their planetary masses (Brogi et al. 2012, 2013, 2014, Rodler et al. 2012, Guilluy et al. 2019); a unique quality of high-resolution spectroscopy.

Assuming that in atmospheres at $T > 1000 \text{ K}$, carbon and oxygen atoms are primarily locked up in CO and H₂O (ignoring CH₄ that can become abundant in carbon-rich atmospheres), atmospheric retrieval analyses can constrain the C/O ratios, which proposedly can shed light on planetary formation processes (Öberg et al. 2011, 2023). However, care has to be taken in comparing results between different planets, since different assumptions in the retrieval set-ups (such as free chemistry, chemical equilibrium, or the presence of clouds) may bias the results. One could argue that the fact that most results are close to the solar C/O value (0.55) indicates that HRS atmospheric retrieval analyses are rather reliable. Interestingly, some C/O ratios derived from JWST observations deviate significantly from solar (i.e. $C/O \sim 0.1$ for HD 209458 b; Xue et al. 2024). Ramkumar et al. (2023) find a C/O ratio consistent with solar for the UHJ MASCARA-1 b, as do Line et al. (2021) for WASP-77A b ($C/O = 0.59 \pm 0.08$), while Bazinet et al. (2024) find a slightly elevated value for HIP 65A b. Brogi et al. (2023) and Lesjak et al. (2023) derive C/O values consistent with 0.75 for WASP-18 b and WASP 43 b respectively, while the non-detection of H₂O in tau Bootis b points to a $C/O > 0.6$ (Pelletier et al. 2021). However, by accounting for undetectable oxygen due to thermal dissociation Brogi et al. (2023) derive $C/O < 0.34$.

Other molecules than CO and H₂O are more rarely detected with HRS. The hydroxyl radical OH, which is the expected photodissociation product of H₂O, was first found in the dayside spectrum of the UHJ WASP-33 b (Nugroho et al. 2021), and confirmed by Cont et al. (2022a). Landman et al. (2021) detect OH in the transmission spectrum of WASP-76 b, confirmed by Cheverall et al. (2023). Retrieval analysis of WASP-33 b by Finnerty et al. (2023) implies that OH is significantly more abundant than H₂O, suggesting the latter

is almost completely photodissociated and showing how general assumptions on chemical and physical atmospheric processes can strongly bias retrieved C/O ratios. HCN is detected in the transmission spectrum of HD 189733 b (Cabot et al. 2019) and HD 209458 b (Hawker et al. 2018, Giacobbe et al. 2021), and tentatively in WASP-76 b (Sánchez-López et al. 2022a).

Metal hydrides and oxides are very prominent in the spectra of late M-dwarfs and Brown Dwarfs, and could therefore also be expected to be present in the atmospheres of irradiated gas giants. E.g. Titanium-oxide (TiO) and Vanadium-oxide (VO) have been proposed as high-altitude absorbers to cause thermal inversion layers (Fortney et al. 2008). However, detection of such molecules has been problematic due to sub-optimal line lists (Hoeijmakers et al. 2015, de Regt et al. 2022), and possibly because they are cold-trapped on the nightside of hot Jupiters (e.g. Parmentier et al. 2013). The quest for TiO in the dayside spectrum of WASP-33 b serves as an example of how elusive observational evidence for hydrides and oxides have been. TiO was first detected by Nugroho et al. (2017). An attempt to confirm this detection with an improved line list using the same data set provided no conclusive evidence (Serindag et al. 2021), neither did Herman et al. (2020). Cont et al. (2021) provide some evidence for TiO, while Yang et al. (2024) report a non-detection. Reports of detections and non-detections seem to come and go, although Prinoth et al. (2023) claim a 6.6σ TiO detection in the transmission spectrum of WASP189 b. Pelletier et al. (2023) present an exciting detection of VO, while Flagg et al. (2023) find evidence for CrH. The most extensive search for a metal hydride, FeH, involved transmission spectra of twelve planets by Kesseli et al. (2020), finding no signals, corresponding to abundance upper limits of $<10^{-7}$ for most planets. As FeH is a powerful surface-gravity indicator, it is not seen in the spectra of red giant stars. Since transmission spectroscopy probes low atmospheric pressures like those for the photospheres of red giants, it may only be present deeper in the atmosphere.

Species CH_4 , NH_3 , and C_2H_2 , have so far only been claimed to be detected using a 4m-class telescope (Basilicata et al. 2024, Guilluy et al. 2019, Giacobbe et al. 2021). However, such detections have been met with skepticism, because the combined detections of these molecules are difficult to explain chemically and some are expected to be significantly less abundant than CO and H_2O in hot Jupiter atmospheres. Indeed some of these measurements have recently been refuted (Blain et al. 2024).

3.2. Atmospheric temperature structure

HRS phase curve spectroscopy is a very powerful tool to constrain the atmospheric temperature structure of extrasolar planets. Theoretical considerations and early spectroscopy with the Spitzer Space Telescope (e.g. Burrows et al. 2007, Fortney et al. 2008, Knutson et al. 2008) initiated a discussion about the possible prevalence of thermal inversion layers within the photospheres of hot Jupiters. Such inversions are present in most solar-system planets (albeit not all in their photospheres). The power of high-resolution spectroscopy comes from the fact that in the case of a thermal inversion individual lines are seen in emission, which turned out not to be the case for most hot Jupiters (e.g. Schwarz et al. 2015).

Figure 7 shows the current results from HRS dayside spectroscopy. Seventeen hot Jupiters and ultra-hot Jupiters have detections from H_2O , CO, and/or iron. All observed hot Jupiters show absorption lines and have non-inverted photospheres, while all observed

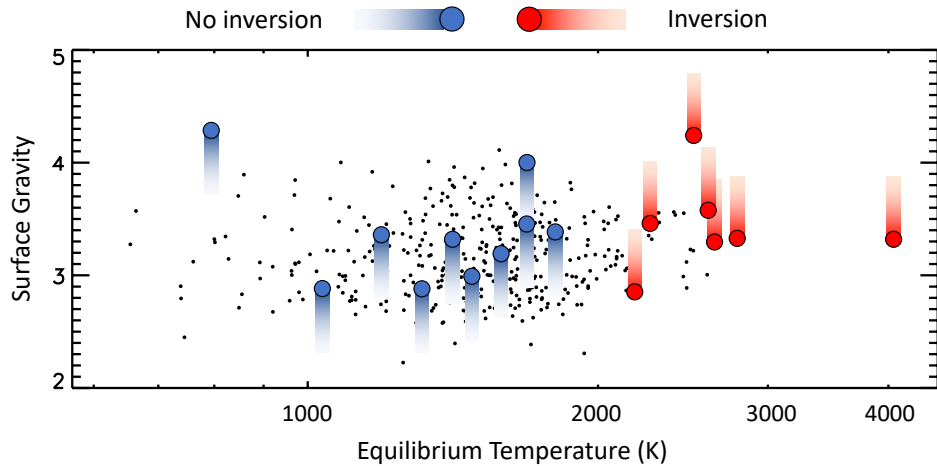


Figure 7

Exoplanets with atomic or molecular detections in their dayside spectra, showing either absorption lines indicative of non-inverted atmospheres (blue symbols), or emission lines implying thermal inversions (red). A clear dichotomy is visible at $T_{\text{eq}} \approx 2000$ K. For non-transiting planets a radius of $1.25 R_{\text{Jup}}$ was assumed. The black dots indicate the general population of transiting gas giants as in Figure 5. References: Pino et al. (2020); Guilluy et al. (2019); Piskorz et al. (2018); Bazinet et al. (2024); Brogi et al. (2023); Ramkumar et al. (2023); Brogi et al. (2012, 2013, 2014); Brogi & Line (2019); de Kok et al. (2013); Yan et al. (2020, 2022a,b, 2023); Birkby et al. (2013, 2017); Line et al. (2021)

Ultra-Hot Jupiters ($T_{\text{eq}} > 2000$ K) exhibit emission lines and have thermal inversions. For a thermal inversion to be present, stellar radiation needs to be absorbed at high altitude. This is most likely caused by species that are efficient absorbers at wavelengths where the host star radiates most of its energy, i.e. the uv/optical wavelength regime. While metal-oxides, in particular TiO and VO, have been proposed to play this role, they appear not to be prominent absorbers in Hot Jupiters and Ultra-Hot Jupiters. Although Sodium absorbs in the optical, it is not present specifically at $T_{\text{eq}} > 2000$ K. It has therefore been proposed that iron and other metals, which characteristically are spectroscopically active in the photospheres of UHJs, may be driving the inversions (e.g. Lothringer & Barman 2019, Yan et al. 2020).

3.3. Atmospheric dynamics, rotation, and outflows

Brown (2001) already advocated more than two decades ago that HRS would be a powerful tool to study atmospheric dynamics. It is indeed an area of research that is unique to this type of observation. The short-period planets that are probed today through transmission and phase curve spectroscopy are expected to be tidally locked, implying that they should have equatorial spin velocities in the range of $1-10 \text{ km sec}^{-1}$, which is accessible through line-broadening (e.g. Brogi et al. 2016). In addition, the planetary rotation and strong stellar irradiation are expected to drive complex atmospheric dynamics. 3-Dimensional

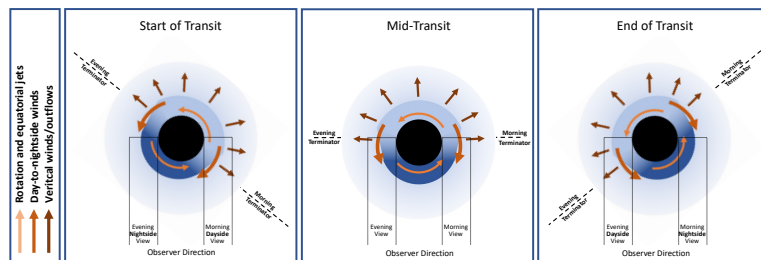


Figure 8

Schematic representation of different dynamical effects probed by transmission HRS, with the planet moving from left to right over the stellar surface. These include planet rotation and equatorial jets, day-to-nightside winds, and outflows leading to atmospheric loss. The viewing angle on the terminator region changes during transit. In the first part of the transit the nightside and dayside of the evening and morning limb are probed respectively, and vice versa at the end of the transit.

global circulation models, also including effects like magnetic drag, are developed to capture such effects and link them to state-of-the-art HRS observations (e.g. Showman et al. 2008, Rauscher & Menou 2010, Showman et al. 2013, Parmentier et al. 2013, Kempton et al. 2014, Belts et al. 2022). Fig. 8 illustrates the different effects to which HRS is potentially sensitive. Planetary rotation with strong stellar forcing is expected to induce equatorial jets that amplify line broadening. Global day-to-nightside winds may transport heat from the dayside to the nightside, which will blueshift transmission lines. In addition, strong stellar irradiation may induce vertical Parker-type winds leading to outflows and atmospheric loss. For the most extreme close-in planets (in terms of a/R_*) the orientation of the planet changes significantly during transit, meaning that different parts of the evening and morning limbs can be studied, resulting in fascinating effects (Ehrenreich et al. 2020).

Day-to-nightside winds Winds that travel from the dayside to the nightside result in a global blueshift of transmission lines. Their velocities are thought to result from a balance between the day/night temperature difference and dissipation mechanisms (e.g. Miller-Ricci Kempton & Rauscher 2012). First evidence of such winds, although at low significance, was presented by Snellen et al. (2010) using CO transmission lines in HD 209458 b. Before conclusions can be drawn from Doppler shift measurements of transmission lines, it must be realised that several effects can influence such observations. The orbital ephemeris needs to be well constrained. For a planet in a 2-day orbit around a solar-type star, a 1 minute error in transit-timing results in a 0.4 km s^{-1} error in the expected radial velocity of the planet, while an error in eccentricity of 0.01 can change the planet's expected velocity during transit by 1 km s^{-1} . Also, the system velocity can be difficult to determine for a fast-rotating star. The stellar gravitational redshift (0.6 km s^{-1} for our Sun) needs to be taken into account, as well as the possible blueshift due to convection cells. If elemental transitions are used that are also present in the stellar atmosphere, such as sodium or iron, an imperfect correction for the Doppler shadow and/or CLV effects may also affect wind measurements.

Reports of day-to-nightside winds have been rather scattered so far, mostly focusing on a single elemental species or molecule for a single planet. Uncertainties are difficult to assess,

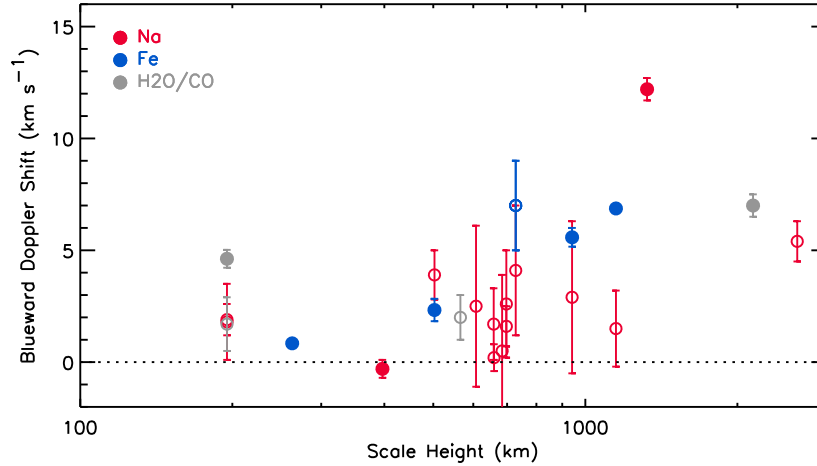


Figure 9

Day-to-nightside winds, as derived from Doppler shifts in transmission spectra, as function of atmospheric scale height. Data points in blue, green and grey are based on Fe, Na, and CO/H₂O respectively, and open circles if their uncertainties are $> 1 \text{ km s}^{-1}$. Although this is a very heterogeneous and incomplete sample, those planets with larger scale heights appear to have, on average, larger day-to-nightside winds. Data from: Langeveld et al. (2022), Gandhi et al. (2023b), Pai Asnodkar et al. (2022), Boucher et al. (2021, 2023), Louden & Wheatley (2015), Brogi et al. (2016), Snellen et al. (2010), Mounzer et al. (2022), Seidel et al. (2023b), Chen et al. (2020a), Wyttenbach et al. (2017), Rahmati et al. (2022)

with different studies of the same planet, even using the same species, sometimes resulting in significantly different wind speeds. Pai Asnodkar et al. (2022) show that even variability may play a role, with four measurements of iron in the transmission spectrum of KELT-9 b taken at different epochs resulting in blueshifts ranging from 4 to 11 km s^{-1} . There have only been a few systematic studies of wind effects in exoplanet atmospheres. Notably, Langeveld et al. (2022) studied ten hot Jupiters and ultra-hot Jupiters in sodium to find blueshifts up to 5 km s^{-1} , but all-bar-one within 2σ from zero – hence barely significant. The retrieval study by Gandhi et al. (2023b) of six ultra-hot Jupiters show them all to have a net blueshift, from $< 1 \text{ km s}^{-1}$ for MASCARA-2 b to 7 km s^{-1} for WASP-76 b, mostly at higher statistical significances.

Figure 9 is an attempt to reveal a pattern in the very heterogeneous and incomplete data on atmospheric winds, based on different atmospheric species. Warm and fluffy planets possibly exhibit stronger winds: all planets with measured winds $> 5 \text{ km s}^{-1}$ have atmospheric scale heights $> 700 \text{ km}$.

Rotation, equatorial jets and time-resolved spectroscopy While day-to-nightside winds are expected to dominate at low pressures high-up in hot-Jupiter atmospheres, most heat transport from the day to nightside is predicted to come from equatorial jets deeper in the atmosphere. Indeed, space-based thermal phase-curve observations of hot Jupiters often show (e.g. Knutson et al. 2007) that their hottest parts are significantly offset from a planet’s substellar point. HRS observations can directly probe these equatorial jets through

line broadening in addition to what is expected from bulk rotation of a tidally locked planet (e.g. Louden & Wheatley 2015, Brogi et al. 2016). However, different contributions from the leading and trailing limbs and contributions from the day-to-nightside winds, thermal broadening, and possible residuals from the RM effect, can significantly complicate such analyses. It is therefore very helpful to add extra information using time-resolved transit spectroscopy. Contributions from the leading (morning side) and trailing (evening side) limb can be isolated by focusing on the ingress and egress transmission spectrum respectively. In this way, Louden & Wheatley (2015) derive wind velocities on the leading and trailing limb of HD 189733 b that are consistent with predictions from atmospheric circulation models and can be understood as a combination of tidally locked planetary rotation and an eastward equatorial jet. Seidel et al. (2020, 2021) retrieved wind patterns, speeds, and temperature profiles from the line shape of the sodium doublet of the ultra-hot Jupiter WASP-76 b, showing that this is best fit with a uniform day-to-nightside wind and a significant vertical wind (see below). More recently, they used the unprecedented collecting area of the four VLT telescopes combined with ESPRESSO's 4UT mode to probe the sodium line in the ultra-hot Jupiter WASP-121 b (Seidel et al. 2023a) and identify a high-velocity component during egress interpreted as an equatorial day-to-night side wind across the evening limb.

Ehrenreich et al. (2020) realised that for planets in particularly close-in orbits, i.e. with small a/R_* (ratio of orbital distance to stellar radius), also the orientation of the planet changes significantly during transit. Due to this *Ehrenreich Effect*, the viewing angle of WASP-76 b varies by about 30° from ingress to egress (see Figure 8). It means that early on in the transit, the transmission spectrum probes on the morning limb the atmospheric dayside of the planet, and on the evening limb the nightside. Late in the transit this is reversed and the dayside evening limb and nightside morning limb are probed. Since contributions from both limbs can be separated because of their different Doppler shifts (due to planet rotation), the planet atmosphere can be traced from day to night-side on the evening and morning side. For WASP-76 b Ehrenreich et al. (2020) show that this results in a transmission signal in iron that increases significantly in strength and blueshift during transit (observation confirmed by Kesseli & Snellen 2021), interpreted as due to a lack of iron on the morning-nightside due to rain-out. Wardenier et al. (2021) show using 3D Monte Carlo radiative transfer modelling that the signal could also be caused by a substantial temperature asymmetry. Gandhi et al. (2022) conducted an atmospheric retrieval analysis separately for the morning and evening terminator regions finding evidence for both a lower iron abundance and lower temperature at the morning limb.

While WASP 76 b is the optimal target to probe the Ehrenreich Effect (among all studied Ultra-Hot Jupiters), and iron the optimal species, similar effects have been detected for other metals and other planets (e.g. Bourrier et al. 2020, Stangret et al. 2020, Hoeijmakers et al. 2020, Kesseli et al. 2022).

In addition to time-resolved transmission spectroscopy, emission spectroscopy can also provide information about heat circulation in combination with global circulation models (e.g. Pino et al. 2022, van Sluijs et al. 2023).

Outflows and atmospheric loss In the years after the first detection of an exoplanet atmosphere (Charbonneau et al. 2002), the archetypical transiting planets HD 209458 b and HD 189733 b were shown to exhibit Lyman alpha absorption at levels of a few percent during transit (Vidal-Madjar et al. 2003, Lecavelier Des Etangs et al. 2010), caused by a

significant halo of exospheric hydrogen. The warm Neptune GJ 436 b was found to have such halo extending as a cometary tail around the planet causing a 50% transit depth (Ehrenreich et al. 2015). Unfortunately, probing hydrogen through Lyman alpha is challenging due to geocoronal absorption which blocks all potential signals near zero velocity, and absorption by the interstellar medium beyond the Local Bubble (30 - 100 pc). Transmission signals by hydrogen from higher energy levels, such as H-alpha (Yan & Henning 2018), other Balmer lines (Wytttenbach et al. 2020, Yan et al. 2021), and even Paschen-beta (Sánchez-López et al. 2022b) are accessible with HRS and point to exospheric gas associated to atmospheric escape, but seem restricted to planets with the highest temperatures (Zhang et al. 2022).

The seminal work by Seager & Sasselov (2000) predicted the presence of helium absorption at 1083 nm in the transmission spectra of hot Jupiters. After some failed attempts to detect this transition, it was overlooked for almost two decades until interest was rejuvenated by Oklopčić & Hirata (2018) and subsequently observed with HST (Spake et al. 2018) as a direct probe of atmospheric loss. Since it is in a wavelength region relatively free of telluric absorption, ground-based HRS has proven to be a very powerful technique to probe its spatial and dynamical structure (Allart et al. 2018, Nortmann et al. 2018). This has revolutionised the study of atmospheric escape, although interpretation of the 1083 nm helium line and conversion to atmospheric losses is less straightforward than that for Lyman-alpha. The helium line originates from an excited metastable 2^3S state for which the population is governed by the radiation field of the host star: while extreme-ultraviolet flux ionises the helium ground state, mid-ultraviolet flux ionises the metastable state (Oklopčić 2019). Close-in planets around K-stars are expected to show the strongest helium absorption while those orbiting early-type stars, despite probably having high mass-loss rates, may show no signal since the metastable state is not sufficiently populated (e.g KELT-9b; Nortmann et al. 2018).

About a dozen planets have been detected in He I, some at very high signal to noise. Both the warm Saturns WASP-69 b and WASP-107 b, located near the edge of the evaporation desert, are shown to have strong absorption signatures with blueshifts of several km s^{-1} and post-transit absorption pointing to comet-like tails. (Nortmann et al. 2018, Allart et al. 2019). For the latter it is estimated that its extended thermosphere fills half of the Roche lobe with an estimated escape rate of meta-stable helium of 10^6 g s^{-1} (Allart et al. 2019). Recently, the cometary tail of WASP-69 b was found to extend to 7.5 planetary radii behind the planet (Tyler et al. 2024). Helium absorption signals can be significantly more extended and complex than this. HAT-P-67 b is exhibiting helium absorption in a large *leading* trail up to 130 planetary radii (necessarily observed over multiple nights; Gully-Santiago et al. 2024). Giant tidal tails of escaping helium have been found both leading and trailing the hot Jupiter HAT-P-32 b (Zhang et al. 2023c) spanning a projected length over 53 planetary radii. It is the intricate interplay between orbital shear, day/night side mass-loss asymmetries and confinement by the stellar wind that is expected to determine the spatial and dynamical morphology of exospheric helium (McCann et al. 2019). By the absence of any stellar wind, atmospheric loss from the planet dayside and nightside will cause a leading and trailing tail respectively due to orbital shear. A strong stellar wind will push any material into a cometary tail behind the planet. Zhang et al. (2020) suggest that the 1083 nm helium line may also be observed as airglow emission away from transit, but that this may require one of the upcoming extremely large telescopes. Helium studies have also been extended to mini-Neptunes (e.g. Zhang et al. 2023a).

3.4. Reflected-light searches

The field of exoplanet atmospheric characterisation once started with attempts to use ground-based HRS observations to probe reflected light, i.e. starlight scattered by planet atmospheres (Charbonneau et al. 1999, Collier Cameron et al. 1999, e.g.). Unfortunately, progress in this particular avenue has been very difficult ever since. While scattered light signals could in principle be as high as $\sim 10^{-4}$ for highly reflective (i.e. cloudy) atmospheres, Hot Jupiters turn out to have very low geometric albedos. Many studies have focused on the tau Bootis system (Charbonneau et al. 1999, Leigh et al. 2003, Hoeijmakers et al. 2018b) because both star and planet are tidally locked. This means that the star is stationary in the planet rest frame, cancelling out the velocity broadening in the reflected light spectrum and maximising a potential atmospheric signal (see also Spring et al. 2022).

Martins et al. (2015) provided evidence for a reflected light signal from 51 Peg b, pointing to a planet radius of $1.9 R_{\text{Jup}}$ and a high geometric albedo of 0.5. However, subsequent studies have not been able to confirm the signal (Spring et al. 2022). It is well possible that HRS reflected light detections will need to wait for the future ELTs. In particular the combination of HRS with high-contrast imaging probing neighbouring stars will be orders of magnitudes more sensitive to scattered light signals, and will be able to probe a new regime of cooler planets that are expected to have significantly higher geometric albedos than Hot Jupiters (Lovis et al. 2017).

3.5. Chromatic Doppler Shadow measurements

Originally proposed two decades ago (Snellen 2004, Dreizler et al. 2009), the RM effect or Doppler shadow can in principle also be used to probe exoplanet atmospheres. At wavelengths where the effective planet size (due to extra atmospheric absorption) is larger, the amplitude of the RM effect and Doppler shadow will also be larger. In measuring the amplitude of the RM effect as function of wavelength a transmission spectrum can be constructed. In this way, Di Gloria et al. (2015) reconstructed the broadband transmission spectrum of HD 189733 b showing evidence, albeit at low significance, for a Rayleigh scattering slope similar to that found using HST (Sing et al. 2011). Independent observations and analyses come to comparable conclusions (Cristo et al. 2022). For HD 209458 b, a remarkable similarity was found between the broadband RM-transit spectrum and that from HST by Santos et al. (2020). Borsa et al. (2019, 2021) found chromatic RM effects for ultra-hot Jupiters, but do not present transmission spectra.

Analysis of the chromatic Doppler shadow remains highly challenging. While based on shape deformations of stellar lines, these same lines may also be present in the planet transmission spectrum (as in the case of sodium, or any metal lines in the case of UHJs), highly complicating the analysis. Depending on the orbital configuration (i.e. spin-orbital alignment) and intrinsic properties of a planet's atmospheric absorption, the strength of the Doppler shadow may significantly vary during transit. This is most apparent when the planetary absorption and Doppler shadow overlap in velocity. These specific epochs are often left out of transmission spectroscopic analyses. However, with the limited lifetime of HST, the chromatic Doppler shadow or RM effect may at some point be the only way to obtain information on blue-optical broadband transmission spectra in the near future.

4. Results on wide-separation exoplanets

Compared to HRS transit and phase curve measurements, HRS combined with high-contrast imaging is still in its relative infancy. First observations of this type were performed at medium spectral resolution, such as the important work by Konopacky et al. (2013), while Snellen et al. (2014) showed its potential by measuring the radial orbital velocity and $v \sin i$ of the Super-Jupiter β Pictoris b. In this section I will highlight some of the state-of-the-art observations, focusing on the first results from KPIC on Keck, and CRIRES+.

The larger the angular distance between planet and host star, the more accurately the planet spectrum can be separated from that of the star. In many cases, the high-resolution spectra that are obtained with this technique are of significantly better quality than transmission or phase-curve spectra. In this section, some recent results are also included from isolated brown dwarfs for which the spectra reach signal-to-noise ratios of >50 per spectral resolution element. In addition to giving potential insights into different formation pathways for brown dwarfs and planets, such observations serve as an ideal benchmark to test the accuracy and robustness of analysis techniques, and to gauge the level of detail that can be retrieved in the case of future high-quality exoplanet spectra.

4.1. Molecular abundances and atmospheric temperature structure

In the last 2-3 years, HRS studies of directly imaged planets and brown dwarfs have not only resulted in detections of many molecular species, but also in stringent constraints on abundances and temperature-pressure profiles. About two-dozen substellar objects have now been targeted with HRS at high signal-to-noise allowing reliable retrieval of atmospheric parameters. We are at the start of a wave of many such investigations which so far have mainly targeted atmospheres in K-band where H_2O and CO are the two dominant contributors for hot/warm objects >1500 K, with an increasing contribution from CH_4 and NH_3 towards lower temperatures (e.g. Wang et al. 2021, Xuan et al. 2022, Costes et al. 2024, de Regt et al. 2024). The hotter targets also show clear absorption by hydrogen fluoride (HF) and several atomic species such as sodium, calcium, and titanium (González Picos et al. 2024).

Figure 10 shows an overview of a heterogeneous sample of young and older field brown dwarfs and super Jupiters for which metallicities and C/O ratios have been measured. Since these are significantly more massive than Jupiter ($10 - 50 M_{\text{Jup}}$) it may not be surprising that their metallicities are broadly consistent with that of our Sun, except for Beta Pictoris b and HD 984 b, which appear to have a lower metal content (Landman et al. 2024, Costes et al. 2024). The metallicities of the Super-Jupiters seem on average somewhat lower than those of the brown dwarfs, but this is unlikely to be statistically significant. They have generally lower-quality spectra resulting in larger error bars and therefore may be biased. Also, the well known $\log(g)$ -metallicity correlation adds to the uncertainty. While C/O ratios could potentially provide insights in their formation processes, almost all objects are consistently measured to be within the C/O=0.5 – 0.65 range.

As a detailed case study, the work by de Regt et al. (2024) is discussed, who obtained a K-band spectrum of the $T=1400$ K field brown dwarf DENIS J0255-4700 at a signal-to-noise of 40 per resolution element as part of the CRIRES+ SupJup Survey. They compared atmospheric retrievals using three different set ups: 1) Free chemistry in which the abundances of relevant chemicals are constant with pressure but otherwise unconstrained; 2) Equilibrium chemistry in which the chemical abundances at each pressure are set by the

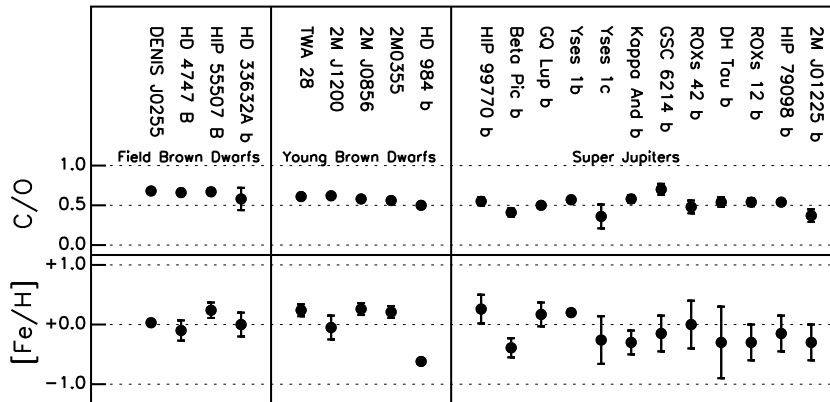


Figure 10

HRS atmospheric retrieval results on C/O ratio and metallicity (derived from C/H) as present in the literature, for field brown dwarfs, young brown dwarfs, and Super-Jupiters. For some measurements the error bars are smaller than the symbol sizes. Data and references are provided in Supplementary Table 2.

metallicity, C/O ratio and temperature; and 3) Quenched equilibrium chemistry in which the abundances follow chemical equilibrium down to a certain pressure, below which the abundances are forced to be constant. The physical idea is that below this quench pressure (so, higher up in the atmosphere) the vertical mixing time scales are shorter than the chemical time scales such that the chemical abundances are governed by the circumstances at the quench pressure. Interestingly, the high data quality allows distinctions to be made between these scenarios. The free chemistry and quench-pressure set-up result in a very similar solution in temperature/pressure profile, chemical abundances, and C/O ratio. The un-quenched chemical equilibrium model provides a significantly worse fit, resulting in a different metallicity and C/O ratio. Basically, the relatively small methane signal pushes the chemical equilibrium model to higher temperatures. At lower signal-to-noise, one may have chosen a model with the lowest number of parameters (i.e. following the Bayesian Information Criterion), which is the chemical equilibrium model, possibly skewing the retrieved parameters. In more extreme cases, the lack of methane, while it is expected at the derived atmospheric temperatures, points to quenching (e.g. Zhang et al. 2024b).

Atmospheric retrieval set-ups also allow for the introduction of clouds, either grey or physically motivated (e.g. MgSiO_3 , Fe, etc.). However, so far, most retrieval analyses find little evidence for significant cloud opacity. Finding evidence for clouds is generally challenging for HRS observations over a relatively narrow wavelength range, where slight changes in the temperature structure can mimic clouds. Most analyses have so far been performed in K-band which probes relatively high altitudes and clouds may be present below the photosphere (Xuan et al. 2022). J and H-band HRS spectra should be significantly more sensitive to cloud layers. As shown by de Regt et al. (2024), the K-band spectrum of DENIS J0255 provides no statistical evidence for cloud opacity, but the cloud-free model-flux at J-band is a factor ~ 3 higher than measured by 2MASS photometry, meaning that clouds indeed need to be present but possibly below the K-band photosphere.

High signal-to-noise spectra also allow detailed modelling of the temperature structure, e.g. by parametrising the T/p profile with temperature gradients (Zhang et al. 2023b) to retrieve the radiative-convective boundary (Marley & Robinson 2015), as is done for GQ Lupi b (Gonzalez Picos et al. 2024, submitted). In addition, the retrieval of a slight deviation from the adiabatic temperature gradient at high pressure suggests the presence of non-adiabatic convection or the cloud-P/T degeneracy (e.g. Tremblin et al. 2019). An additional effect that has been identified in high signal-to-noise spectra is veiling (Folha & Emerson 1999). Some young substellar objects may have a circum-planetary disk that significantly contributes to the observed spectrum as a continuum source, making the object spectral lines appear shallower. E.g. significant veiling at $\sim 14\%$ of the continuum flux at K-band is measured for the young brown dwarf 2M J1200 (González Picos et al. 2024), and it is found to be very prominent in the K-band spectrum of the GQ Lupi host star at $>50\%$ level (Gonzalez Picos et al 2024, submitted).

The higher the data quality, the more complex the modelling needs to be to appropriately fit the data. While K-band HRS monitoring of the nearby brown dwarf Luhman 16B resulted in the first brown-dwarf Doppler-imaging map (Crossfield 2014), De Regt et al. (in preparation) show that at $S/n \geq 100/\text{pixel}$, HRS becomes sensitive to spatial inhomogeneities. This can reveal the presence of cloud bands and vortices in single-epoch observations by deviation from the expected rotational line-broadening profile from a homogeneous limb-darkened disk. Other model refinements are possibly required at the highest levels of data quality, such as molecular abundance variations with altitude due to non-LTE processes.

4.2. Orbital and Rotational Dynamics

The atmospheric retrieval analyses as discussed above also provide the projected rotational broadening, or $v \sin i$, of the observed targets. While $\sin i$ is unknown for most objects, for a randomly oriented sample, the true spin velocity is on average only 15% higher. Also, only 15% of a sample of randomly oriented targets is expected to have $i < 30^\circ$ with true spin velocities that are larger by a factor two or more than the measured $v \sin i$. In principle, their inclinations can be determined if they show significant flux variability that lead to the derivation of their spin period. In combination with constraints on their orbital inclination, the radial component of the obliquity can be determined, as shown by Bryan et al. (2020) who derive a planetary obliquity for the Super-Jupiter 2M J0122 b of at least 49_{-21}^{+27} degrees.

Investigating the rotation rates of exoplanets may shed light on their formation mechanisms, how their angular momentum is set via interaction with a circum-planetary disk through magnetic coupling, and possibly altered later through collisions or gravitational tides (Bryan et al. 2018, 2020). For those substellar objects with measured $v \sin i$ the radii can be estimated from their derived surface brightness, flux density, and distance to Earth. Figure 11 shows the measured $v \sin i$ as function of radius for field brown dwarfs, young brown dwarfs, and Super-Jupiters. In any evolutionary sequence it would be expected that the youngest, bloated objects rotate the slowest, subsequently cool and contract over time and spin up. Although this is a very heterogeneous sample, all-but-one objects with $R > 1.75 R_{\text{Jup}}$ have a $v \sin i < 10 \text{ km s}^{-1}$, while most targets with $R < 1.75 R_{\text{Jup}}$ exhibit significantly higher spin velocities. In the future, large and complete samples of brown dwarfs and gas-giant exoplanets for which the ages, radii, and masses can be derived more accurately, will provide interesting constraints on the evolution of angular momentum of these objects. While the

current sample is a varied assortment, and the uncertainties in radii are large, the distribution of $v \sin i$ for Jupiter-size objects seems to have a larger spread than expected from a random distribution in $\sin i$ alone. Objects of the same size seem to have significantly different rotation velocities.

In addition to rotational broadening, atmospheric retrievals also reveal the radial velocity of the exoplanet, and if that of the host star is determined, the radial component of its orbital velocity. This can be used to constrain the planet orbital elements, as shown by Schwarz et al. (2016) for GQ Lup b. There is growing evidence that some Super-Jupiters at wide orbits have high eccentricities that point to a formation in a close-in orbit and subsequent planet-planet interactions (e.g. Dupuy et al. 2023).

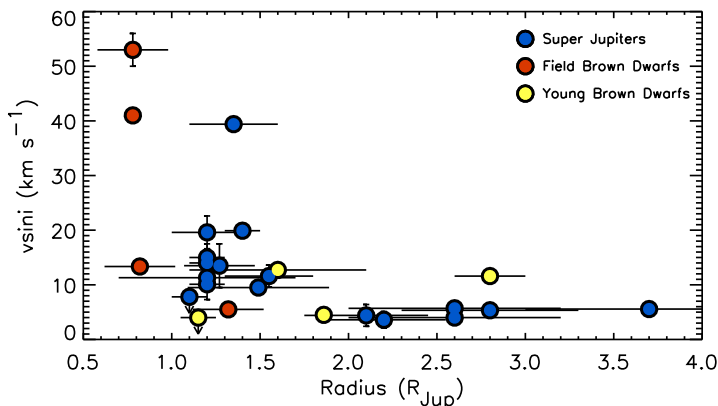


Figure 11

HRS measurements of $v \sin i$ as function of estimated object radius for field brown dwarfs (red), young brown dwarfs (yellow) and Super-Jupiters (blue). Data and references are provided in Supplementary Table 2.

4.3. Isotope measurements

The ability to detect individual isotopologues and determine isotope ratios in exoplanet atmospheres opens up a new pathway to constrain planet formation and evolutionary processes (e.g. Mollière & Snellen 2019, Morley et al. 2019). Figure 12 shows the derived $^{12}\text{C}/^{13}\text{C}$ isotope ratios from HRS retrieval analysis for brown dwarfs, Super-Jupiters and hot Jupiters. Again, this is a very heterogeneous sample and could be biased in multiple ways. The $^{12}\text{C}/^{13}\text{C}$ ratio for VHS1256 b is derived from medium-resolution JWST spectroscopy, which also detects ^{17}O and ^{18}O (Gandhi et al. 2023a). The dashed and dotted lines indicate the average isotope ratio in the interstellar medium and the solar system respectively. The first exoplanet isotope measured as presented by Zhang et al. (2021) showed the atmosphere of YSES 1 b to be rich in carbon-13 with $^{12}\text{C}/^{13}\text{C} = 31_{-10}^{+17}$, but higher-quality HRS observations now point to $^{12}\text{C}/^{13}\text{C} = 88 \pm 13$ (Zhang et al. 2024a). Also, two independent HRS studies of GQ Lup b point to significantly different isotope ratios. It implies that these measurements are still challenging, that uncertainties may be underestimated, and/or that systematic effects are yet not well understood. Taking the measurements in Fig. 12 at face value, the Super-Jupiters appear to have slightly lower carbon isotope ratios

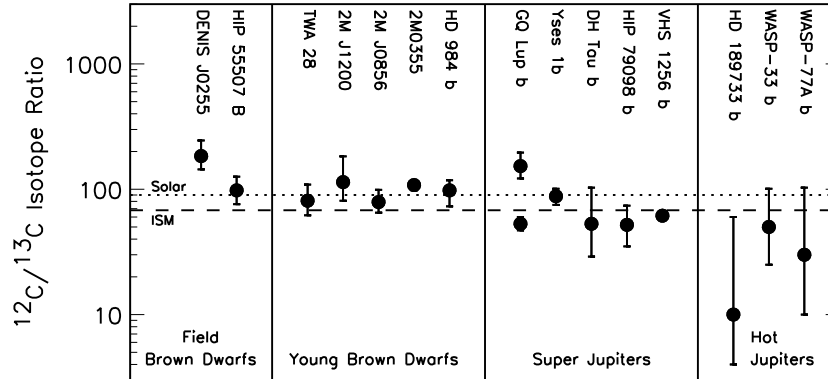


Figure 12

Carbon isotope ratios presented in the literature for field brown dwarfs, young brown dwarfs, Super-Jupiters, and Hot Jupiters. Data and references are provided in Supplementary Table 2.

than the brown dwarfs, while the three hot Jupiters have even lower ratios. However, these latter measurements are presented as tentative detections and may suffer from detection bias. It is fair to say that it is too early to draw any conclusions, but that a new avenue of exoplanet atmospheric characterisation is opening up.

5. Synergies with JWST spectroscopy of exoplanets

Only two years after the start of its science operations, it is clear that the James Webb Space Telescope is revolutionising the field of extrasolar planets. While transmission spectroscopy of Hot Jupiters has revealed previously undetected species such as CO_2 and SO_2 (e.g. Powell et al. 2024), it also pioneers detailed atmospheric characterisation of smaller and cooler planets. For example, SO_2 and silicate clouds are detected in a warm Neptune (Dyrek et al. 2024), strong evidence is found for a secondary atmosphere around the hot rocky exoplanet 55 Cancri e (Hu et al. 2024), and mid-infrared secondary eclipse observations with MIRI are constraining the dayside temperatures of the Earth-size planets in the TRAPPIST-1 system (e.g. Zieba et al. 2023).

The great sensitivity of JWST relative to ground-based observations, in particular at wavelength beyond $2.5 \mu\text{m}$, means that it will most likely require the enormous collecting area of the ELTs for HRS to play a competitive role in the thermal infrared. We will discuss how HRS will break new ground in the era of the ELTs in the next section. However, there are exciting synergies with JWST with current 8-10m class telescopes, and domains where ground-based HRS continues to provide uniquely new insights.

Some spectral regions can be particularly crowded with absorption features from a variety of species such that low resolution spectroscopy cannot unambiguously identify the absorbing molecules or atoms. The optical/near-infrared spectra of Ultra-Hot Jupiters are very rich in metals (see Fig. 6) which are challenging to individually identify with JWST's limited spectral resolution. Also the velocity structure of exospheric helium, as a probe of atmospheric loss process, is uniquely accessible with ground-based HRS. The spectral signature of CO, consisting of series of regularly spaced lines, is particularly favourable

for HRS. While CO was the first molecule detected in the transmission spectrum of HD 209458 b (Snellen et al. 2010), it is barely seen in JWST/NIRSpec transmission observations of the planet (Xue et al. 2024). Also, CO is not seen in JWST/NIRISS secondary eclipse observations of WASP-18 b (Coulombe et al. 2023), while clearly detected in ground-based HRS observations with IGRINS (Brogi et al. 2023) allowing for the planet's C/O ratio to be measured.

The study of minor isotopes has exciting synergetic opportunities between HRS and JWST observations. While ground-based HRS has so far focused on ^{13}CO , JWST observations have revealed $^{15}\text{NH}_3$ (Barrado et al. 2023) and oxygen-17 and oxygen-18 isotopes of CO (Gandhi et al. 2023a), and possibly deuterium (in CH_3D) is within reach (Morley et al. 2019). Future will tell whether trends in isotope ratios will emerge that will shed new light on planet formation and evolutionary processes.

The spectral resolution of JWST instrumentation is insufficient to directly probe any dynamics, but phase curve analyses of close-in planets still provide crucial information on day-nightside heat distribution, heat transportation, and longitudinal distribution of molecular gases. These can be coupled to direct measurements of wind-speeds and morning/evening terminator retrievals from HRS to build up a holistic picture of hot Jupiter atmospheres. In a similar way, JWST variability monitoring can be directly linked to HRS $v \sin i$ and line profile variation measurements to constrain cloud cover distributions and planet obliquities.

While HRS preserves information on individual line profiles and probes atmospheres at relatively low pressures, JWST observations preserve continuum information more accurately, have generally a wider spectral range and probe deeper parts of the atmosphere. Combining the two can be a powerful way to constrain a planet's properties (Brogi et al. 2017, Gandhi et al. 2019). Smith et al. (2024) used a joint retrieval framework on secondary-eclipse JWST and pre- and post-eclipse HRS observations on the hot Jupiter WASP-77A b, showing that both data sets are consistent and that molecular abundances as well as vertical thermal structure could be determined at higher precision than by using either data set individually. It is also interesting to apply ground-based cross-correlation HRS techniques to medium-resolution JWST observations. Snellen et al. (2017) proposed to apply such a technique to MIRI/MRS spectra of Proxima Cen b to reveal potential signatures from CO_2 , which seems technically within the realm of possibilities (Deming et al. 2024b). Esparza-Borges et al. (2023) apply cross-correlation techniques on WASP-39 b NIRSPEC data showing it to be more powerful than a conventional analysis, unequivocally showing the presence of CO and providing evidence for ^{13}CO .

It remains a fact that JWST is pushing exoplanet characterisation to a regime that currently seems out of reach of ground-based HRS. It remains to be seen how far HRS transmission spectroscopy can be pushed to cooler planets on wider orbits. The question is whether ground-based HRS observers should be more bold and daring. It is important to know whether detections of CO_2 and SO_2 are currently too difficult from the ground, or whether simply nobody tried. Maybe HRS observers (and telescope allocation committees) have been too conservative and not willing to invest significantly more observing time on individual targets to break new ground. The same can be argued for the new discoveries of young embedded planets, such as PDS 70 (Haffert et al. 2019, Cugno et al. 2021) and AB Aur (Currie et al. 2022), for which HRS observations could constrain the dynamics and chemistry of their accretion environment.

6. Future opportunities with the ELT

As discussed in Section 2, with the advent of the ELTs we will enter a new era of HRS exoplanet characterisation. The increase in collecting area (and detection speed) of up to a factor 25 will increase the sensitivity of HRS transmission and phase-curve observations by up to a factor 5. It means that high-resolution emission and transmission spectra of hot gas giant planets will be obtained of similar quality as those currently obtained for brown dwarfs (Prinoth et al. 2024), but that also temporal information, e.g. during ingress, egress or specific orbital phases will provide detailed information of the temperature structure, gaseous content and dynamics in specific areas of their atmospheres. While transmission spectroscopy of cooler exoplanets often result in flat transmission spectra due to clouds and hazes, it is expected that ELT-HRS can probe such atmospheres above their clouds to determine their gaseous contents and climates (e.g. Gandhi et al. 2020, Hood et al. 2020, Grasser et al. 2024). Also, it may well be that HRS with the ELTs will break the degeneracies originating from stellar activity that currently plague JWST transmission observations (e.g. Deming et al. 2024a).

It is high-contrast HRS where enormous gains will be made, increasing the detection speed by three orders of magnitude and unlocking exoplanets at unprecedentedly small angular distances from their host stars. While METIS (Brandl et al. 2021), first-generation instrument at the ELT, will have $R=100,000$ integral field and long-slit spectroscopy between 3 and 5 μm at near-maximum Strehl ratios, second-generation instrument ANDES (which will exhibit a small IFU) will serve the optical and near-infrared regime at similar spectral resolution (Marconi et al. 2022). While current instrumentation is generally limited to such contrasts that it can *only* probe young planets that are still sufficiently warm from their formation, the ELTs are expected to push into the regime that scattered light from planets around our nearest neighbours can be studied. Many such planets are already known to exist through radial velocity or astrometric studies and many more are expected from population statistics. The mid-infrared detection of a temperate Super-Jupiter around one of the most close-by solar-type stars Epsilon Indi A using JWST (Matthews et al. 2024a) is a milestone. Excitingly, its thermal emission at 10 μm is visible in archival VLT data. Knowing the orders-of-magnitude increase in sensitivity that will be achieved with the ELTs, such a planet can be detected within minutes of observing time. It may already be detectable at $\sim 4 \mu\text{m}$ using HRS with current telescopes to characterise the molecular content of its atmosphere, illustrating the enormous potential of the ELTs.

6.1. Towards Earth-like planets

The ultimate goal for the ELTs, and arguably the exoplanet field as a whole, is to characterise Earth-like planets and establish whether they could be habitable and show signs of life. This involves a cascade of questions about temperate rocky planets: Do these planets have an atmosphere? What are their chemical constituents? What are their climates like? Is there any water? Are there biomarker gases present? Are these biomarkers indeed due to biological activity? This final question will be extremely challenging to address. Temperate rocky planets in red dwarf systems are the most accessible for characterisation, and JWST is paving the way by addressing the first and possibly the second question above for a subset of the TRAPPIST-1 planets (e.g. Zieba et al. 2023). If their atmospheric conditions are favourable, HRS transmission spectroscopy with the ELT will be sensitive to molecular absorption including molecular oxygen, although the latter will be challenging (Snellen et al.

2013, Rodler & López-Morales 2014, Currie et al. 2023).

However, it is high-contrast spectroscopy that will be the real game-changer for the characterisation of other Earths. METIS HRS-IFU mode will be able to target Proxima Cen b and probe the atmosphere for H₂O, CO₂, and CH₄ in L and M band. If the atmosphere is water-rich, deuterium and the D/H ratio may be determined via HDO measurements at 3.5 μm (Mollière & Snellen 2019) and shed light on its history of atmospheric loss. ANDES with its small IFU mode, will determine its albedo over the optical and near-infrared, constrain cloud cover, and probe gaseous species, including molecular oxygen (Lovis et al. 2017, Palle et al. 2023, Vaughan et al. 2024).

The results of the first and second generation of ELT instrumentation will greatly depend on the specific properties of rocky planets around M-dwarfs, such as their geometric albedo (reflected light is expected to dominate over thermal emission at < 5μm). Results on Proxima b will also largely be governed by the contrast limits that can be reached with adaptive optics, which is more challenging at shorter wavelengths. Dedicated instrumentation will be needed to facilitate extreme adaptive optics for the ELTs at the level of the state-of-the-art high-contrast imaging facilities at current 8-10m telescopes. This instrumentation is currently being developed for the European ELT (PCS; Kasper et al. 2021) and the GMT (GMagAO-X; Males et al. 2022). It is still an open question at what spectral resolution these instruments will operate. Landman et al. (2023) presented detailed simulations for gas giant planets and showed that medium resolution is optimal for this type of planet from a signal-to-noise point of view. However, in the case of reflected light, it is probably necessary to spectrally separate the Doppler shifted planet spectrum from direct starlight to avoid confusion from near-identical telluric and stellar features, pushing requirements to the high-resolution regime. It is envisaged that the high spectral and spatial resolution at extreme contrast levels will eventually allow the characterisation of up to tens of temperate rocky planets around nearby M-dwarfs (Hardegree-Ullman et al. 2024).

Current projections suggest that the 10^{9–10} contrasts needed to detect and characterise Earth-twins around solar type stars will not be reached with ground-based instrumentations and will require space observatories such as the proposed Habitable Worlds Observatory (HWO⁴) or a space interferometer at mid-infrared wavelengths (e.g. the LIFE mission⁵). It has been contemplated whether space-based high-resolution spectroscopy would be an interesting avenue to pursue, knowing the technical challenges. Evidently, the absence of telluric contamination removes an important reason to use HRS. While the dominated noise source for ground-based observations is that from leaked starlight, this is likely to be detector noise in the case of space-based observations. Hence, without new technologies that will significantly reduce detector noise, high spectral resolution (spreading the light over many more detector pixels) is less favourable. Taking these considerations into account it is apparent that R~100–5000 spectroscopy will have the largest discovery space and characterisation power for Earth-twins (Wang et al. 2017) using HWO-type space observatories. The power of high-resolution spectroscopy is closely tied to its use with the largest ground-based telescopes.

⁴<https://habitableworldsobservatory.org/home>

⁵<https://life-space-mission.com>

DISCLOSURE STATEMENT

The author is not aware of any affiliations, memberships, funding, or financial holdings that might be perceived as affecting the objectivity of this review.

ACKNOWLEDGMENTS

The author is grateful to all the stimulating discussions with many colleagues. In particular, Michael Line, Matteo Brogi, Jayne Birkby, Paul Mollière, Sid Gandhi, Natalie Grasser, Dario González Picos, Yapeng Zhang, and Sam de Regt are thanked for carefully reading of the manuscript and their comments.

LITERATURE CITED

- Allart R, Bourrier V, Lovis C, Ehrenreich D, Aceituno J, et al. 2019. *A&A* 623:A58
- Allart R, Bourrier V, Lovis C, Ehrenreich D, Spake JJ, et al. 2018. *Science* 362(6421):1384–1387
- Allart R, Pino L, Lovis C, Sousa SG, Casasayas-Barris N, et al. 2020. *A&A* 644:A155
- Azevedo Silva T, Demangeon ODS, Santos NC, Allart R, Borsa F, et al. 2022. *A&A* 666:L10
- Barrado D, Mollière P, Patapis P, Min M, Tremblin P, et al. 2023. *Nature* 624(7991):263–266
- Basilicata M, Giacobbe P, Bonomo AS, Scandariato G, Brogi M, et al. 2024. *arXiv e-prints* :arXiv:2403.01527
- Baudino JL, Bézard B, Boccaletti A, Bonnefoy M, Lagrange AM, Galicher R. 2015. *A&A* 582:A83
- Bazinet L, Pelletier S, Benneke B, Salinas R, Mace GN. 2024. *arXiv e-prints* :arXiv:2403.07983
- Bello-Arufe A, Cabot SHC, Mendonça JM, Buchhave LA, Rathcke AD. 2022. *AJ* 163(2):96
- Bello-Arufe A, Knutson HA, Mendonça JM, Zhang MM, Cabot SHC, et al. 2023. *ApJ* 166(2):69
- Belts H, Rauscher E, Roman MT, Guillat A. 2022. *AJ* 163(1):35
- Ben-Yami M, Madhusudhan N, Cabot SHC, Constantinou S, Piette A, et al. 2020. *ApJL* 897(1):L5
- Benneke B, Wong I, Piaulet C, Knutson HA, Lothringer J, et al. 2019. *ApJL* 887(1):L14
- Bernath PF. 2020. *JQSRT* 240:106687
- Birkby JL. 2018. *arXiv e-prints* :arXiv:1806.04617
- Birkby JL, de Kok RJ, Brogi M, de Mooij EJW, Schwarz H, et al. 2013. *MNRAS* 436:L35–L39
- Birkby JL, de Kok RJ, Brogi M, Schwarz H, Snellen IAG. 2017. *ApJ* 153(3):138
- Blain D, Landman R, Mollière P, Dittmann J. 2024. *arXiv e-prints* :arXiv:2408.13536
- Borsa F, Allart R, Casasayas-Barris N, Taberner H, Zapatero Osorio MR, et al. 2021. *A&A* 645:A24
- Borsa F, Fossati L, Koskinen T, Young ME, Shulyak D. 2021. *Nature Astronomy* 6:226–231
- Borsa F, Rainer M, Bonomo AS, Barbato D, Fossati L, et al. 2019. *A&A* 631:A34
- Borsato NW, Hoeijmakers HJ, Prinoth B, Thorsbro B, Forsberg R, et al. 2023. *A&A* 673:A158
- Boucher A, Darveau-Bernier A, Pelletier S, Lafreniere D, Artigau E, et al. 2021. *ApJ* 162(6):233
- Boucher A, Lafreniere D, Pelletier S, Darveau-Bernier A, Radica M, et al. 2023. *MNRAS* 522(4):5062–5083
- Bourrier V, Ehrenreich D, Lendl M, Cretignier M, Allart R, et al. 2020. *A&A* 635:A205
- Bowesman CA, Yurchenko SN, Tennyson J. 2024. *Molecular Physics* 122(7-8):e2255299
- Bowler BP, Liu MC, Dupuy TJ, Cushing MC. 2010. *ApJ* 723(1):850–868
- Brandl B, Bettonvil F, van Boekel R, Glauser A, Quanz S, et al. 2021. *The Messenger* 182:22–26
- Brogi M, de Kok RJ, Albrecht S, Snellen IAG, Birkby JL, Schwarz H. 2016. *ApJ* 817(2):106
- Brogi M, de Kok RJ, Birkby JL, Schwarz H, Snellen IAG. 2014. *A&A* 565:A124
- Brogi M, Emeka-Okafor V, Line MR, Gandhi S, Pino L, et al. 2023. *ApJ* 165(3):91
- Brogi M, Line M, Bean J, Désert JM, Schwarz H. 2017. *The Astrophysical Journal Letters* 839(1):L2
- Brogi M, Line MR. 2019. *ApJ* 157(3):114
- Brogi M, Snellen IAG, de Kok RJ, Albrecht S, Birkby J, de Mooij EJW. 2012. *Nature* 486(7404):502–504

- Brogi M, Snellen IAG, de Kok RJ, Albrecht S, Birkby JL, de Mooij EJW. 2013. *ApJ* 767(1):27
- Brown TM. 2001. *ApJ* 553(2):1006–1026
- Bryan ML, Benneke B, Knutson HA, Batygin K, Bowler BP. 2018. *Nature Astronomy* 2:138–144
- Bryan ML, Chiang E, Bowler BP, Morley CV, Millholland S, et al. 2020. *AJ* 159(4):181
- Bryan ML, Ginzburg S, Chiang E, Morley C, Bowler BP, et al. 2020. *ApJ* 905(1):37
- Burningham B, Marley MS, Line MR, Lupu R, Visscher C, et al. 2017. *MNRAS* 470(1):1177–1197
- Burrows A, Hubeny I, Budaj J, Knutson HA, Charbonneau D. 2007. *ApJL* 668(2):L171–L174
- Cabot SHC, Madhusudhan N, Hawker GA, Gandhi S. 2019. *MNRAS* 482(4):4422–4436
- Carteret Y, Bourrier V, Dethier W. 2024. *A&A* 683:A63
- Casasayas-Barris N, Pallé E, Stangret M, Bourrier V, Tabernero HM, et al. 2021. *A&A* 647:A26
- Casasayas-Barris N, Pallé E, Yan F, Chen G, Kohl S, et al. 2019. *A&A* 628:A9
- Cauley PW, Wang J, Shkolnik EL, Ilyin I, Strassmeier KG, et al. 2021. *ApJ* 161(3):152
- Cegla HM, Lovis C, Bourrier V, Beeck B, Watson CA, Pepe F. 2016. *A&A* 588:A127
- Charbonneau D, Allen LE, Megeath ST, Torres G, Alonso R, et al. 2005. *ApJ* 626(1):523–529
- Charbonneau D, Brown TM, Latham DW, Mayor M. 2000. *ApJL* 529(1):L45–L48
- Charbonneau D, Brown TM, Noyes RW, Gilliland RL. 2002. *ApJ* 568(1):377–384
- Charbonneau D, Noyes RW, Korzennik SG, Nisenson P, Jha S, et al. 1999. *ApJL* 522(2):L145–L148
- Chauvin G, Lagrange AM, Dumas C, Zuckerman B, Mouillet D, et al. 2004. *A&A* 425:L29–L32
- Chazelas B, Lovis C, Blind N, Kühn J, Genolet L, et al. 2020. *RISTRETTO: a pathfinder instrument for exoplanet atmosphere characterization*. In *Adaptive Optics Systems VII*, eds. L Schreiber, D Schmidt, E Vernet, vol. 11448 of *Society of Photo-Optical Instrumentation Engineers (SPIE) Conference Series*
- Chen G, Casasayas-Barris N, Pallé E, Welbanks L, Madhusudhan N, et al. 2020a. *A&A* 642:A54
- Chen G, Casasayas-Barris N, Pallé E, Yan F, Stangret M, et al. 2020b. *A&A* 635:A171
- Cheverall C, Madhusudhan N. 2024. *arXiv e-prints* :arXiv:2403.18894
- Cheverall CJ, Madhusudhan N, Holmberg M. 2023. *MNRAS* 522(1):661–677
- Collier Cameron A, Horne K, Penny A, James D. 1999. *Nature* 402(6763):751–755
- Cont D, Yan F, Reiners A, Casasayas-Barris N, Mollière P, et al. 2021. *A&A* 651:A33
- Cont D, Yan F, Reiners A, Nortmann L, Molaverdikhani K, et al. 2022a. *A&A* 668:A53
- Cont D, Yan F, Reiners A, Nortmann L, Molaverdikhani K, et al. 2022b. *A&A* 657:L2
- Cooper CS, Showman AP. 2006. *ApJ* 649(2):1048–1063
- Costes JC, Xuan JW, Vigan A, Wang J, D’Orazi V, et al. 2024. *A&A* 686:A294
- Coulombe LP, Benneke B, Challener R, Piette AAA, Wisner LS, et al. 2023. *Nature* 620(7973):292–298
- Cristo E, Santos NC, Demangeon O, Martins JHC, Figueira P, et al. 2022. *A&A* 660:A52
- Crossfield IJM. 2014. *A&A* 566:A130
- Cugno G, Patapis P, Stolker T, Quanz SP, Boehle A, et al. 2021. *A&A* 653:A12
- Currie MH, Meadows VS, Rasmussen KC. 2023. *PSJ* 4(5):83
- Currie T, Lawson K, Schneider G, Lyra W, Wisniewski J, et al. 2022. *Nature Astronomy* 6:751–759
- Czesla S, Klocová T, Khalafinejad S, Wolter U, Schmitt JHMM. 2015. *A&A* 582:A51
- de Kok RJ, Brogi M, Snellen IAG, Birkby J, Albrecht S, de Mooij EJW. 2013. *A&A* 554:A82
- de Regt S, Gandhi S, Snellen IAG, Zhang Y, Ginski C, et al. 2024. *A&A* 688:A116
- de Regt S, Kesseli AY, Snellen IAG, Merritt SR, Chubb KL. 2022. *A&A* 661:A109
- Deibert EK, de Mooij EJW, Jayawardhana R, Turner JD, Ridden-Harper A, et al. 2021. *ApJL* 919(2):L15
- Delorme JR, Jovanovic N, Echeverri D, Mawet D, Kent Wallace J, et al. 2021. *JATIS* 7:035006
- Deming D, Brown TM, Charbonneau D, Harrington J, Richardson LJ. 2005a. *ApJ* 622(2):1149–1159
- Deming D, Currie M, Meadows V, Peacock S. 2024a. *Bias-free Transit Spectroscopy of Terrestrial Exoplanets Using the ELTs*. In *American Astronomical Society Meeting Abstracts*, vol. 244 of *American Astronomical Society Meeting Abstracts*
- Deming D, Fu G, Bouwman J, Dicken D, Espinoza N, et al. 2024b. *PASP* 136(8):084402

- Deming D, Seager S, Richardson LJ, Harrington J. 2005b. *Nature* 434(7034):740–743
- Deming D, Wilkins A, McCullough P, Burrows A, Fortney JJ, et al. 2013. *ApJ* 774(2):95
- Di Gloria E, Snellen IAG, Albrecht S. 2015. *A&A* 580:A84
- Dreizler S, Reiners A, Homeier D, Noll M. 2009. *A&A* 499(2):615–621
- Dupuy TJ, Liu MC, Evans EL, Best WMJ, Pearce LA, et al. 2023. *MNRAS* 519(2):1688–1694
- Dyrek A, Min M, Decin L, Bouwman J, Crouzet N, et al. 2024. *Nature* 625(7993):51–54
- Ehrenreich D, Bourrier V, Wheatley PJ, Lecavelier des Etangs A, Hébrard G, et al. 2015. *Nature* 522(7557):459–461
- Ehrenreich D, Lovis C, Allart R, Zapatero Osorio MR, Pepe F, et al. 2020. *Nature* 580(7805):597–601
- Esparza-Borges E, López-Morales M, Adams Redai JI, Pallé E, Kirk J, et al. 2023. *ApJL* 955(1):L19
- Finnerty L, Schofield T, Sappéy B, Xuan JW, Ruffio JB, et al. 2023. *ApJ* 166(1):31
- Fisher C, Hoeijmakers HJ, Kitzmann D, Márquez-Neila P, Grimm SL, et al. 2020. *ApJ* 159(5):192
- Flagg L, Turner JD, Deibert E, Ridden-Harper A, de Mooij E, et al. 2023. *ApJL* 953(2):L19
- Folha DFM, Emerson JP. 1999. *A&A* 352:517–531
- Fortney JJ, Lodders K, Marley MS, Freedman RS. 2008. *ApJ* 678(2):1419–1435
- Fossati L, Biassoni F, Cappello GM, Borsa F, Shulyak D, et al. 2023. *A&A* 676:A99
- Gandhi S, Brogi M, Webb RK. 2020. *MNRAS* 498(1):194–204
- Gandhi S, de Regt S, Snellen I, Zhang Y, Rugers B, et al. 2023a. *ApJ* 957(2):L36
- Gandhi S, Kesseli A, Snellen I, Brogi M, Wardenier JP, et al. 2022. *MNRAS* 515(1):749–766
- Gandhi S, Kesseli A, Zhang Y, Louca A, Snellen I, et al. 2023b. *ApJ* 165(6):242
- Gandhi S, Madhusudhan N. 2018. *MNRAS* 474(1):271–288
- Gandhi S, Madhusudhan N, Hawker G, Piette A. 2019. *AJ* 158(6):228
- Giacobbe P, Brogi M, Gandhi S, Cubillos PE, Bonomo AS, et al. 2021. *Nature* 592(7853):205–208
- Gibson NP, de Mooij EJW, Evans TM, Merritt S, Nikolov N, et al. 2019. *MNRAS* 482(1):606–615
- Gibson NP, Merritt S, Nugroho SK, Cubillos PE, de Mooij EJW, et al. 2020. *MNRAS* 493(2):2215–2228
- Gibson NP, Merritt S, Nugroho SK, Cubillos PE, de Mooij EJW, et al. 2020. *MNRAS* 493(2):2215–2228
- Gibson NP, Nugroho SK, Lothringer J, Maguire C, Sing DK. 2022. *MNRAS* 512(3):4618–4638
- González Picos D, Snellen IAG, de Regt S, Landman R, Zhang Y, et al. 2024. *arXiv e-prints*:arXiv:2407.07678
- Gordon IE, Rothman LS, Hill C, Kochanov RV, Tan Y, et al. 2017. *JQSRT* 203:3–69
- Grasser N, Snellen IAG, Landman R, Picos DG, Gandhi S. 2024. *A&A* 688:A191
- GRAVITY Collaboration, Nowak M, Lacour S, Mollière P, Wang J, et al. 2020. *A&A* 633:A110
- Gray DF. 1997. *Nature* 385(6619):795–796
- Guillot T. 2010. *A&A* 520:A27
- Guilluy G, Sozzetti A, Brogi M, Bonomo AS, Giacobbe P, et al. 2019. *A&A* 625:A107
- Gully-Santiago M, Morley CV, Luna J, MacLeod M, Oklopčić A, et al. 2024. *AJ* 167(4):142
- Haffert SY, Bohn AJ, de Boer J, Snellen IAG, Brinchmann J, et al. 2019. *Nature Astronomy* 3:749–754
- Hardegree-Ullman KK, Apai D, Haffert SY, Schlecker M, Kasper M, et al. 2024. *arXiv e-prints*:arXiv:2405.11423
- Hargreaves RJ, Gordon IE, Rey M, Nikitin AV, Tyuterev VG, et al. 2020. *ApJS* 247(2):55
- Hawker GA, Madhusudhan N, Cabot SHC, Gandhi S. 2018. *ApJL* 863(1):L11
- Herman MK, de Mooij EJW, Jayawardhana R, Brogi M. 2020. *ApJ* 160(2):93
- Hoeijmakers HJ, Cabot SHC, Zhao L, Buchhave LA, Tronsgaard R, et al. 2020. *A&A* 641:A120
- Hoeijmakers HJ, de Kok RJ, Snellen IAG, Brogi M, Birkby JL, Schwarz H. 2015. *A&A* 575:A20
- Hoeijmakers HJ, Ehrenreich D, Heng K, Kitzmann D, Grimm SL, et al. 2018a. *Nature* 560(7719):453–455
- Hoeijmakers HJ, Ehrenreich D, Kitzmann D, Allart R, Grimm SL, et al. 2019. *A&A* 627:A165

- Hoeijmakers HJ, Kitzmann D, Morris BM, Prinoth B, Borsato N, et al. 2022. *arXiv e-prints* :arXiv:2210.12847
- Hoeijmakers HJ, Snellen IAG, van Terwisga SE. 2018b. *A&A* 610:A47
- Holmberg M, Madhusudhan N. 2022. *ApJ* 164(3):79
- Hood CE, Fortney JJ, Line MR, Martin EC, Morley CV, et al. 2020. *AJ* 160(5):198
- Hood T, Debras F, Moutou C, Klein B, Tremblin P, et al. 2024. *arXiv e-prints* :arXiv:2403.19434
- Hsu CC, Wang JJ, Xuan JW, Ruffio JB, Morris E, et al. 2024. *ApJ* 971(1):9
- Hu R, Bello-Arufe A, Zhang M, Paragas K, Zilinskas M, et al. 2024. *Nature* 630(8017):609–612
- Irwin PGJ, Teanby NA, de Kok R, Fletcher LN, Howett CJA, et al. 2008. *JQSRT* 109:1136–1150
- Jiang Z, Wang W, Zhao G, Zhai M, Shi Y, et al. 2023. *ApJ* 165(6):230
- Kasper M, Cerpa Urta N, Pathak P, Bonse M, Nousiainen J, et al. 2021. *The Messenger* 182:38–43
- Kawahara H, Hirano T. 2014. *arXiv e-prints* :arXiv:1409.5740
- Kawahara H, Kawashima Y, Masuda K, Crossfield IJM, Pannier E, van den Bekerom D. 2022. *ApJS* 258(2):31
- Kempton EMR, Perna R, Heng K. 2014. *ApJ* 795(1):24
- Kesseli AY, Snellen IAG. 2021. *The Astrophysical Journal Letters* 908(1):L17
- Kesseli AY, Snellen IAG, Alonso-Floriano FJ, Mollière P, Serindag DB. 2020. *ApJ* 160(5):228
- Kesseli AY, Snellen IAG, Casasayas-Barris N, Mollière P, Sánchez-López A. 2022. *ApJ* 163(3):107
- Kitzmann D, Heng K, Rimmer PB, Hoeijmakers HJ, Tsai SM, et al. 2018. *apj* 863(2):183
- Knutson HA, Charbonneau D, Allen LE, Burrows A, Megeath ST. 2008. *ApJ* 673(1):526–531
- Knutson HA, Charbonneau D, Allen LE, Fortney JJ, Agol E, et al. 2007. *Nature* 447(7141):183–186
- Konopacky QM, Barman TS, Macintosh BA, Marois C. 2013. *Science* 339(6126):1398–1401
- Kotani T, Kawahara H, Ishizuka M, Jovanovic N, Vievard S, et al. 2020. *Extremely high-contrast, high spectral resolution spectrometer REACH for the Subaru Telescope*. In *Adaptive Optics Systems VII*, eds. L Schreiber, D Schmidt, E Vernet, vol. 11448 of *Society of Photo-Optical Instrumentation Engineers (SPIE) Conference Series*
- Kreidberg L, Bean JL, Désert JM, Benneke B, Deming D, et al. 2014. *Nature* 505(7481):69–72
- Lagrange AM, Bonnefoy M, Chauvin G, Apai D, Ehrenreich D, et al. 2010. *Science* 329(5987):57
- Landman R, Snellen IAG, Keller CU, N'Diaye M, Fagginger-Auer F, Desgrange C. 2023. *A&A* 675:A157
- Landman R, Stolker T, Snellen IAG, Costes J, de Regt S, et al. 2024. *A&A* 682:A48
- Landman R, Sánchez-López A, Mollière P, Kesseli AY, Louca AJ, Snellen IAG. 2021. *A&A* 656:A119
- Langeveld AB, Madhusudhan N, Cabot SHC. 2022. *mnras* 514(4):5192–5213
- Lecavelier Des Etangs A, Ehrenreich D, Vidal-Madjar A, Ballester GE, Désert JM, et al. 2010. *A&A* 514:A72
- Leigh C, Collier Cameron A, Horne K, Penny A, James D. 2003. *MNRAS* 344(4):1271–1282
- Lesjak F, Nortmann L, Yan F, Cont D, Reiners A, et al. 2023. *A&A* 678:A23
- Line MR, Brogi M, Bean JL, Gandhi S, Zalesky J, et al. 2021. *Nature* 598(7882):580–584
- Line MR, Fortney JJ, Marley MS, Sorahana S. 2014. *ApJ* 793(1):33
- Lothringer JD, Barman T. 2019. *ApJ* 876(1):69
- Louden T, Wheatley PJ. 2015. *ApJL* 814(2):L24
- Lovis C, Snellen I, Mouillet D, Pepe F, Wildi F, et al. 2017. *A&A* 599:A16
- Madhusudhan N. 2019. *ARA&A* 57:617–663
- Madhusudhan N, Seager S. 2009. *ApJ* 707(1):24–39
- Maguire C, Gibson NP, Nugroho SK, Ramkumar S, Fortune M, et al. 2023. *MNRAS* 519(1):1030–1048
- Maimone MC, Brogi M, Chiavassa A, van den Ancker ME, Manara CF, et al. 2022. *A&A* 667:A106
- Males JR, Close LM, Haffert SY, Guyon O, Gasho V, et al. 2022. *The conceptual design of GMagAO-X: visible wavelength high contrast imaging with GMT*. In *Adaptive Optics Systems VIII*, eds. L Schreiber, D Schmidt, E Vernet, vol. 12185 of *Society of Photo-Optical Instrumentation Engineers (SPIE) Conference Series*

- Malik M, Grosheintz L, Mendonça JM, Grimm SL, Lavie B, et al. 2017. *AJ* 153(2):56
- Marconi A, Abreu M, Adibekyan V, Alberti V, Albrecht S, et al. 2022. *ANDES, the high resolution spectrograph for the ELT: science case, baseline design and path to construction*. In *Ground-based and Airborne Instrumentation for Astronomy IX*, eds. CJ Evans, JJ Bryant, K Motohara, vol. 12184 of *Society of Photo-Optical Instrumentation Engineers (SPIE) Conference Series*
- Marley MS, Robinson TD. 2015. *ARAA* 53:279–323
- Marois C, Macintosh B, Barman T, Zuckerman B, Song I, et al. 2008. *Science* 322(5906):1348
- Martins JHC, Santos NC, Figueira P, Faria JP, Montalto M, et al. 2015. *A&A* 576:A134
- Matthews E, Carter A, Pathak Pea. 2024a. *Nature*
- Matthews SM, Watson CA, de Mooij EJW, Marsh TR, Brogi M, et al. 2024b. *MNRAS* 531(3):3800–3814
- Mawet D, Wizinowich P, Dekany R, Chun M, Hall D, et al. 2016. *Keck Planet Imager and Characterizer: concept and phased implementation*. In *Adaptive Optics Systems V*, eds. E Marchetti, LM Close, JP Véran, vol. 9909 of *Society of Photo-Optical Instrumentation Engineers (SPIE) Conference Series*
- Mayor M, Queloz D. 1995. *Nature* 378(6555):355–359
- McCann J, Murray-Clay RA, Kratter K, Krumholz MR. 2019. *ApJ* 873(1):89
- McKemmish LK, Masseron T, Hoeijmakers HJ, Pérez-Mesa V, Grimm SL, et al. 2019. *MNRAS* 488(2):2836–2854
- Merritt SR, Gibson NP, Nugroho SK, de Mooij EJW, Hooton MJ, et al. 2021. *MNRAS* 506(3):3853–3871
- Miller-Ricci Kempton E, Rauscher E. 2012. *ApJ* 751(2):117
- Mollière P, Wardenier JP, van Boekel R, Henning T, Molaverdikhani K, Snellen IAG. 2019. *A&A* 627:A67
- Mollière P, Snellen IAG. 2019. *A&A* 622:A139
- Moran SE, Stevenson KB, Sing DK, MacDonald RJ, Kirk J, et al. 2023. *ApJL* 948(1):L11
- Morley CV, Skemer AJ, Miles BE, Line MR, Lopez ED, et al. 2019. *ApJL* 882(2):L29
- Mounzer D, Lovis C, Seidel JV, Attia O, Allart R, et al. 2022. *A&A* 668:A1
- Moutou C, Coustenis A, Schneider J, St Gilles R, Mayor M, et al. 2001. *A&A* 371:260–266
- Nortmann L, Pallé E, Salz M, Sanz-Forcada J, Nagel E, et al. 2018. *Science* 362(6421):1388–1391
- Nugroho SK, Gibson NP, de Mooij EJW, Herman MK, Watson CA, et al. 2020a. *The Astrophysical Journal Letters* 898(2):L31
- Nugroho SK, Gibson NP, de Mooij EJW, Watson CA, Kawahara H, Merritt S. 2020b. *MNRAS* 496(1):504–522
- Nugroho SK, Kawahara H, Gibson NP, de Mooij EJW, Hirano T, et al. 2021. *ApJL* 910(1):L9
- Nugroho SK, Kawahara H, Masuda K, Hirano T, Kotani T, Tajitsu A. 2017. *ApJ* 154(6):221
- Öberg KI, Facchini S, Anderson DE. 2023. *ARA&A* 61:287–328
- Öberg KI, Murray-Clay R, Bergin EA. 2011. *ApJL* 743(1):L16
- Oklopčić A. 2019. *ApJ* 881(2):133
- Oklopčić A, Hirata CM. 2018. *ApJL* 855(1):L11
- Pai Asnodkar A, Wang J, Eastman JD, Cauley PW, Gaudi BS, et al. 2022. *ApJ* 163(4):155
- Palle E, Biazzo K, Bolmont E, Molliere P, Poppenhaeger K, et al. 2023. *arXiv e-prints*:arXiv:2311.17075
- Parmentier V, Showman AP, Lian Y. 2013. *A&A* 558:A91
- Pelletier S, Benneke B, Ali-Dib M, Prinoth B, Kasper D, et al. 2023. *Nature* 619(7970):491–494
- Pelletier S, Benneke B, Darveau-Bernier A, Boucher A, Cook NJ, et al. 2021. *ApJ* 162(2):73
- Perryman MAC. 2000. *Reports on Progress in Physics* 63(8):1209–1272
- Pino L, Brogi M, Désert JM, Nascimbeni V, Bonomo AS, et al. 2022. *A&A* 668:A176
- Pino L, Désert JM, Brogi M, Malavolta L, Wyttenbach A, et al. 2020. *ApJL* 894(2):L27
- Piskorz D, Buzard C, Line MR, Knutson HA, Benneke B, et al. 2018. *ApJ* 156(3):133
- Powell D, Feinstein AD, Lee EKH, Zhang M, Tsai SM, et al. 2024. *Nature* 626(8001):979–983

- Prinoth B, Hoeijmakers HJ, Morris BM, Lam M, Kitzmann D, et al. 2024. *arXiv e-prints*:arXiv:2403.08863
- Prinoth B, Hoeijmakers HJ, Pelletier S, Kitzmann D, Morris BM, et al. 2023. *A&A* 678:A182
- Prinoth B, Sedaghati E, Seidel JV, Hoeijmakers HJ, Brahm R, et al. 2024. *AJ* 168(3):133
- Rahmati H, Czesla S, Khalafinejad S, Mollière P. 2022. *A&A* 668:A24
- Ramkumar S, Gibson NP, Nugroho SK, Maguire C, Fortune M. 2023. *MNRAS* 525(2):2985–3005
- Rauscher E, Menou K. 2010. *ApJ* 714(2):1334–1342
- Redfield S, Endl M, Cochran WD, Koesterke L. 2008. *ApJL* 673(1):L87
- Rey M, Nikitin AV, Babikov YL, Tyuterev VG. 2016. *Journal of Mol. Spectroscopy* 327:138–158
- Riaud P, Schneider J. 2007. *A&A* 469(1):355–361
- Rodler F, Kürster M, Barnes JR. 2013. *MNRAS* 432(3):1980–1988
- Rodler F, López-Morales M. 2014. *ApJ* 781(1):54
- Rodler F, Lopez-Morales M, Ribas I. 2012. *ApJL* 753(1):L25
- Rodler F, Lopez-Morales M, Ribas I. 2012. *ApJL* 753(1):L25
- Ruffio JB, Horstman K, Mawet D, Rosenthal LJ, Batygin K, et al. 2023. *AJ* 165(3):113
- Ruffio JB, Macintosh B, Konopacky QM, Barman T, De Rosa RJ, et al. 2019. *AJ* 158(5):200
- Santos NC, Cristo E, Demangeon O, Oshagh M, Allart R, et al. 2020. *A&A* 644:A51
- Schwarz H, Brogi M, de Kok R, Birkby J, Snellen I. 2015. *A&A* 576:A111
- Schwarz H, Ginski C, de Kok RJ, Snellen IAG, Brogi M, Birkby JL. 2016. *A&A* 593:A74
- Seager S, Sasselov DD. 2000. *ApJ* 537(2):916–921
- Seidel JV, Borsa F, Pino L, Ehrenreich D, Stangret M, et al. 2023a. *A&A* 673:A125
- Seidel JV, Cegla HM, Doyle L, Lafarga M, Brogi M, et al. 2022. *MNRAS* 513(1):L15–L19
- Seidel JV, Ehrenreich D, Allart R, Hoeijmakers HJ, Lovis C, et al. 2021. *A&A* 653:A73
- Seidel JV, Ehrenreich D, Pino L, Bourrier V, Lavie B, et al. 2020. *A&A* 633:A86
- Seidel JV, Prinoth B, Knudstrup E, Hoeijmakers HJ, Zanazzi JJ, Albrecht S. 2023b. *A&A* 678:A150
- Serindag DB, Nugroho SK, Mollière P, de Mooij EJW, Gibson NP, Snellen IAG. 2021. *A&A* 645:A90
- Showman AP, Cooper CS, Fortney JJ, Marley MS. 2008. *ApJ* 682(1):559–576
- Showman AP, Fortney JJ, Lewis NK, Shabram M. 2013. *ApJ* 762(1):24
- Sing DK, Fortney JJ, Nikolov N, Wakeford HR, Kataria T, et al. 2016. *Nature* 529(7584):59–62
- Sing DK, Pont F, Aigrain S, Charbonneau D, Désert JM, et al. 2011. *MNRAS* 416(2):1443–1455
- Sing DK, Wakeford HR, Showman AP, Nikolov N, Fortney JJ, et al. 2015. *MNRAS* 446(3):2428–2443
- Smith PCB, Line MR, Bean JL, Brogi M, August P, et al. 2024. *AJ* 167(3):110
- Snellen I, de Kok R, Birkby JL, Brandl B, Brogi M, et al. 2015. *A&A* 576:A59
- Snellen IAG. 2004. *MNRAS* 353(1):L1–L6
- Snellen IAG, Albrecht S, de Mooij EJW, Le Poole RS. 2008. *A&A* 487(1):357–362
- Snellen IAG, Brandl BR, de Kok RJ, Brogi M, Birkby J, Schwarz H. 2014. *Nature* 509(7498):63–65
- Snellen IAG, de Kok RJ, de Mooij EJW, Albrecht S. 2010. *Nature* 465(7301):1049–1051
- Snellen IAG, de Kok RJ, le Poole R, Brogi M, Birkby J. 2013. *ApJ* 764(2):182
- Snellen IAG, Désert JM, Waters LBFM, Robinson T, Meadows V, et al. 2017. *AJ* 154(2):77
- Sousa-Silva C, Al-Refaie AF, Tennyson J, Yurchenko SN. 2015. *MNRAS* 446(3):2337–2347
- Spake JJ, Sing DK, Evans TM, Oklopčić A, Bourrier V, et al. 2018. *Nature* 557(7703):68–70
- Sparks WB, Ford HC. 2002. *ApJ* 578(1):543–564
- Spring EF, Birkby JL, Pino L, Alonso R, Hoyer S, et al. 2022. *A&A* 659:A121
- Stangret M, Casasayas-Barris N, Pallé E, Orell-Miquel J, Morello G, et al. 2022. *A&A* 662:A101
- Stangret M, Casasayas-Barris N, Pallé E, Yan F, Sánchez-López A, López-Puertas M. 2020. *A&A* 638:A26
- Sánchez-López A, Landman R, Mollière P, Casasayas-Barris N, Kesseli AY, Snellen IAG. 2022a. *A&A* 661:A78
- Sánchez-López A, Lin L, Snellen IAG, Casasayas-Barris N, García Muñoz A, et al. 2022b. *A&A* 666:L1

- Taberner HM, Zapatero Osorio MR, Allart R, Borsa F, Casasayas-Barris N, et al. 2021. *A&A* 646:A158
- Tamuz O, Mazeh T, Zucker S. 2005. *MNRAS* 356(4):1466–1470
- Tennyson J, Yurchenko SN. 2021. *Astronomy and Geophysics* 62(6):6.16–6.21
- Tinetti G, Vidal-Madjar A, Liang MC, Beaulieu JP, Yung Y, et al. 2007. *Nature* 448(7150):169–171
- Tremblin P, Padioleau T, Phillips MW, Chabrier G, Baraffe I, et al. 2019. *ApJ* 876(2):144
- Tyler D, Petigura EA, Oklopčić A, David TJ. 2024. *ApJ* 960(2):123
- van Sluijs L, Birkby JL, Lothringer J, Lee EKH, Crossfield IJM, et al. 2023. *MNRAS* 522(2):2145–2170
- Vaughan SR, Birkby JL, Thatte N, Carlotti A, Houllé M, et al. 2024. *MNRAS* 528(2):3509–3522
- Vidal-Madjar A, Désert JM, Lecavelier des Etangs A, Hébrard G, Ballester GE, et al. 2004. *ApJL* 604(1):L69–L72
- Vidal-Madjar A, Lecavelier des Etangs A, Désert JM, Ballester GE, Ferlet R, et al. 2003. *Nature* 422(6928):143–146
- Vigan A, El Morsy M, Lopez M, Otten GPPL, Garcia J, et al. 2024. *A&A* 682:A16
- Wang J, Mawet D, Ruane G, Hu R, Benneke B. 2017. *ApJ* 153(4):183
- Wang JJ, Ruffio JB, Morris E, Delorme JR, Jovanovic N, et al. 2021. *AJ* 162(4):148
- Wardenier JP, Parmentier V, Lee EKH, Line MR, Gharib-Nezhad E. 2021. *MNRAS* 506(1):1258–1283
- Watson CA, de Mooij EJW, Steeghs D, Marsh TR, Brogi M, et al. 2019. *MNRAS* 490(2):1991–2006
- Wiedemann G, Deming D, Bjakker G. 2001. *ApJ* 546(2):1068–1074
- Wolszczan A, Frail DA. 1992. *Nature* 355(6356):145–147
- Wytttenbach A, Lovis C, Ehrenreich D, Bourrier V, Pino L, et al. 2017. *A&A* 602:A36
- Wytttenbach A, Mollière P, Ehrenreich D, Cegla HM, Bourrier V, et al. 2020. *A&A* 638:A87
- Xuan JW, Hsu CC, Finnerty L, Wang J, Ruffio JB, et al. 2024a. *ApJ* 970(1):71
- Xuan JW, Wang J, Finnerty L, Horstman K, Grimm S, et al. 2024b. *ApJ* 962(1):10
- Xuan JW, Wang J, Ruffio JB, Knutson H, Mawet D, et al. 2022. *ApJ* 937(2):54
- Xue Q, Bean JL, Zhang M, Welbanks L, Lunine J, August P. 2024. *ApJL* 963(1):L5
- Yan F, Casasayas-Barris N, Molaverdikhani K, Alonso-Floriano FJ, Reiners A, et al. 2019. *A&A* 632:A69
- Yan F, Henning T. 2018. *Nature Astronomy* 2:714–718
- Yan F, Nortmann L, Reiners A, Piskunov N, Hatzes A, et al. 2023. *A&A* 672:A107
- Yan F, Pallé E, Fosbury RAE, Petr-Gotzens MG, Henning T. 2017. *A&A* 603:A73
- Yan F, Pallé E, Reiners A, Casasayas-Barris N, Cont D, et al. 2022a. *A&A* 661:L6
- Yan F, Pallé E, Reiners A, Molaverdikhani K, Casasayas-Barris N, et al. 2020. *A&A* 640:L5
- Yan F, Reiners A, Pallé E, Shulyak D, Stangret M, et al. 2022b. *A&A* 659:A7
- Yan F, Wytttenbach A, Casasayas-Barris N, Reiners A, Pallé E, et al. 2021. *A&A* 645:A22
- Yang Y, Chen G, Wang S, Yan F. 2024. *ApJ* 167(1):36
- Zahnle KJ, Marley MS. 2014. *ApJ* 797(1):41
- Zhang M, Chachan Y, Kempton EMR, Knutson HA. 2019. *PASP* 131(997):034501
- Zhang M, Knutson HA, Dai F, Wang L, Ricker GR, et al. 2023a. *AJ* 165(2):62
- Zhang Y, González Picos D, de Regt S, Snellen IAG, Gandhi S, et al. 2024a. *arXiv e-prints*:arXiv:2409.16660
- Zhang Y, Snellen IAG, Bohn AJ, Mollière P, Ginski C, et al. 2021. *Nature* 595(7867):370–372
- Zhang Y, Snellen IAG, Mollière P. 2021. *A&A* 656:A76
- Zhang Y, Snellen IAG, Mollière P, Alonso-Floriano FJ, Webb RK, et al. 2020. *A&A* 641:A161
- Zhang Y, Snellen IAG, Wytttenbach A, Nielsen LD, Lendl M, et al. 2022. *A&A* 666:A47
- Zhang Y, Xuan JW, Mawet D, Wang JJ, Hsu CC, et al. 2024b. *AJ* 168(3):131
- Zhang Z, Mollière P, Hawkins K, Manea C, Fortney JJ, et al. 2023b. *AJ* 166(5):198
- Zhang Z, Morley CV, Gully-Santiago M, MacLeod M, Oklopčić A, et al. 2023c. *Science Advances* 9(23):eadf8736

Zhou G, Bayliss DDR. 2012. *MNRAS* 426(3):2483–2488

Zieba S, Kreidberg L, Ducrot E, Gillon M, Morley C, et al. 2023. *Nature* 620(7975):746–749

Žák J, Kabáth P, Boffin HMJ, Ivanov VD, Skarka M. 2019. *ApJ* 158(3):120

Supplementary Tables for *Exoplanet Atmospheres at High Spectral Resolution*

Ignas Snellen, Leiden Observatory, Leiden University,
Postbus 9513, 2300 RA Leiden, The Netherlands

Table 2 Data used to produce Fig. 5, showing planet name, apparent V-band magnitude of the host star, equilibrium temperature, atmospheric scale height, Scale Height Contrast, amplitude of sodium signal, and the literature references. All parameters, except sodium signal, are derived from data in the NASA Exoplanet Archive (<https://exoplanetarchive.ipac.caltech.edu>). Note that the literature measurement of WASP-67 b could not be converted into a transmission signal amplitude.

Planet	V _{star} mag	T _{eq} K	H km	SHC %	Na %	Ref.
HAT-P-67 b	10.1	1930	3570	0.033	–	Bello-Arufe et al. (2023)
HAT-P-70 b	9.5	2550	>190	>0.0030	0.203	Bello-Arufe et al. (2022)
HD 189733 b	7.7	1190	200	0.011	0.39	Langeveld et al. (2022)
HD 209458 b	7.7	1480	570	0.016	<0.41 [†]	Snellen et al. (2008)
KELT-11 b	8.0	1700	2630	0.014	0.5	Mounzer et al. (2022)
KELT-9 b	7.6	4050	730	0.0071	0.16	Langeveld et al. (2022)
MASCARA-2 b	7.6	2260	>290	>0.0060	0.37	Casasayas-Barris et al. (2019)
MASCARA-4 b	8.2	2400	260	0.0031	0.2	Zhang et al. (2022)
WASP 21 b	11.6	1260	700	0.019	1.16	Langeveld et al. (2022)
WASP-121 b	10.5	2450	940	0.022	0.65	Langeveld et al. (2022)
WASP-127 b	10.1	1420	2150	0.046	0.34	Žák et al. (2019)
WASP-166 b	9.4	1270	720	0.0088	0.44	Seidel et al. (2022)
WASP-17 b	11.6	1700	1100	0.027	1.80	Zhou & Bayliss (2012)
WASP-172 b	11.0	1750	1330	0.016	0.30	Seidel et al. (2023b)
WASP-189 b	6.6	2640	500	0.0042	0.13	Langeveld et al. (2022)
WASP-49 b	11.4	1370	660	0.022	2.00	Wytttenbach et al. (2017)
WASP-52 b	12.2	1300	660	0.039	1.30	Chen et al. (2020b)
WASP-69 b	9.9	990	610	0.026	3.28	Langeveld et al. (2022)
WASP-7 b	9.5	1490	400	0.0074	0.50	Rahmati et al. (2022)
WASP-76 b	9.5	2180	1150	0.020	0.47	Langeveld et al. (2022)
WASP-79 b	10.0	1720	680	0.013	1.12	Langeveld et al. (2022)

[†]Conflicting non-detection by Casasayas-Barris et al. (2021)

Table 3 Data used to produce Figures 10, 11, and 12, showing the object name, object type (BS = field brown dwarf; YBD = young brown dwarf; SJ = Super Jupiter), C/O ratio, metallicity, $^{12}\text{CO}/^{13}\text{CO}$ isotope ratio, $v \sin i$, and literature references.

Object	Type	Radius (R_J)	C/O Ratio	C/H	$\frac{^{12}\text{CO}}{^{13}\text{CO}}$	$v \sin i$ (km s^{-1})	Ref.
DENIS J0255	BD	0.78 ± 0.01	0.68 ± 0.005	0.03 ± 0.05	184_{-40}^{+61}	41.0 ± 0.2	de Regt et al. (2024)
TWA 28	YBD	2.8 ± 0.2	0.61 ± 0.02	0.24 ± 0.1	81_{-19}^{+28}	11.6 ± 0.1	González Picos et al. (2024)
2M J0856	YBD	1.86 ± 0.04	0.58 ± 0.01	0.26 ± 0.1	79_{-14}^{+20}	4.5 ± 0.2	González Picos et al. (2024)
HIP 99770 b	SJ	1.1 ± 0.1	0.55 ± 0.05	0.26 ± 0.24		< 7.8	Zhang et al. (2024b)
Beta Pic b	SJ	1.4 ± 0.1	0.41 ± 0.05	-0.39 ± 0.16		19.9 ± 1.0	Landman et al. (2024)
2M0355	YBD	1.15 ± 0.1	0.56 ± 0.02	0.21 ± 0.1	108_{-10}^{+10}	< 4	Zhang et al. (2021)
GQ Lup b	SJ	3.7 ± 0.7	0.50 ± 0.01	0.17 ± 0.2	53_{-7}^{+7}	5.6 ± 0.1	González Picos et al., 2024
YSES 1 b	SJ	2.8 ± 0.5	0.57 ± 0.01	0.20 ± 0.05	153_{-31}^{+48}		Xuan et al. (2024a)
YSES 1 c	SJ	1.2 ± 0.5	0.36 ± 0.15	-0.26 ± 0.4	88_{-13}^{+13}	5.3 ± 0.2	Zhang et al. 2024
HD 984 b	YBD	1.6 ± 0.5	0.50 ± 0.01	-0.62 ± 0.02	98_{-20}^{+25}	11.3 ± 2.1	Zhang et al. 2024
HR 8799 d	SJ	1.2 ± 0.1				12.7 ± 0.03	Costes et al. (2024)
HR 8799 e	SJ	1.2 ± 0.1				10.1 ± 2.8	Wang et al. (2021)
HD 4747 B	BD	0.82 ± 0.2	0.66 ± 0.04	-0.10 ± 0.17		15.0 ± 2.5	Wang et al. (2021)
HIP 55507 B	BD	1.32 ± 0.2	0.67 ± 0.04	0.24 ± 0.13	98_{-22}^{+28}	13.4 ± 1.3	Xuan et al. (2022)
Kappa And b	SJ	1.35 ± 0.25	0.58 ± 0.05	-0.3 ± 0.3		5.5 ± 0.25	Xuan et al. (2024b)
GSC 6214 b	SJ	1.55 ± 0.25	0.70 ± 0.07	-0.15 ± 0.4		39.4 ± 0.9	Xuan et al. (2024a)
ROXs 42B	SJ	2.10 ± 0.25	0.48 ± 0.08	0.0 ± 0.6		11.6 ± 2.0	Xuan et al. (2024a)
DH Tau	SJ	2.6 ± 0.6	0.54 ± 0.06	-0.30 ± 0.30	53_{-24}^{+50}	4.4 ± 2.0	Xuan et al. (2024a)
ROXs 12	SJ	2.2 ± 0.35	0.54 ± 0.05	-0.30 ± 0.30		5.7 ± 1.0	Xuan et al. (2024a)
HIP 79098	SJ	2.6 ± 0.6	0.54 ± 0.03	-0.15 ± 0.3	52_{-17}^{+22}	3.6 ± 1.5	Xuan et al. (2024a)
2M J01225	SJ	1.2 ± 0.2	0.37 ± 0.08			4.0 ± 1.0	Xuan et al. (2024a)
VHS 1256 b	SJ	1.27 ± 0.2				19.6 ± 3.0	Xuan et al. (2024a)
HD 106906 b	SJ	1.49 ± 0.4				13.5 ± 4	Bryan et al. (2018)
HD 33632A B	BD	0.78 ± 0.2	0.58 ± 0.14	0.0 ± 0.2		9.5 ± 0.2	Bryan et al. (2020)
						53 ± 3	Hsu et al. (2024)